CHAPTER 7

RADIATIVE PROCESSES

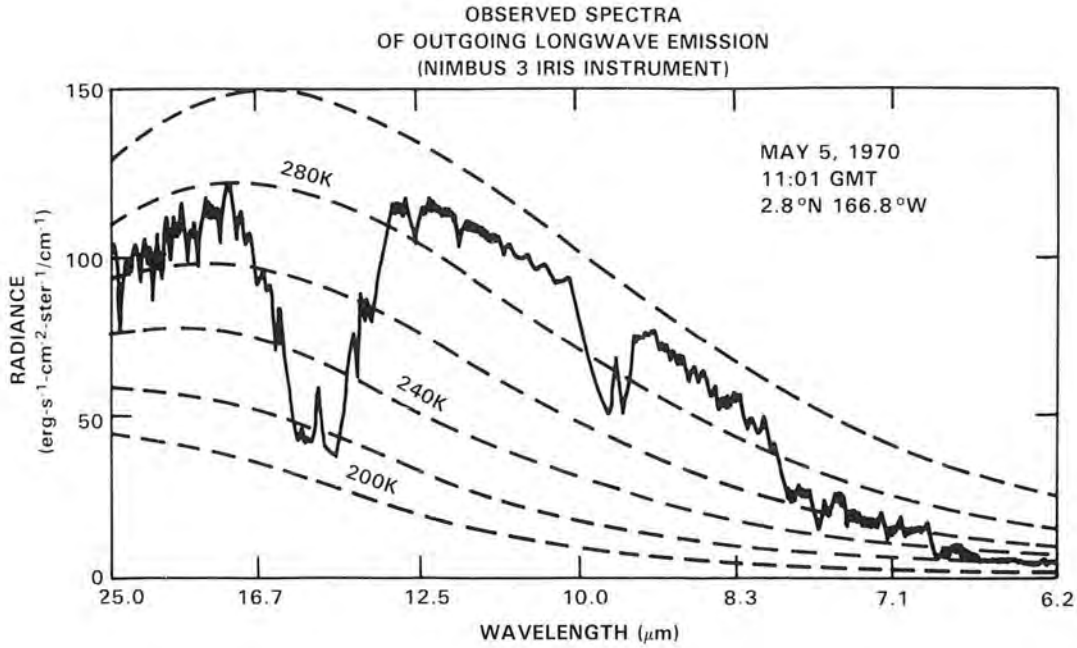

Panel Members

J.E. Frederick and C. Leovy, Co-Chairmen

D.E. Anderson, Jr.
G.P. Anderson
R.E. Dickinson
S.R. Drayson
S. Fels
L.A. Hall
J. Kiehl
J.E. Mentall
G.H. Mount
M. Nicolet
C.D. Rodgers
G. Rottman
P.C. Simon

CHAPTER 7

RADIATIVE PROCESSES: SOLAR AND TERRESTRIAL

TABLE OF CONTENTS

7.0 INTRODUCTION 349

7.1 SOLAR RADIATION AND ITS ABSORPTION IN THE STRATOSPHERE AND MESOSPHERE 349

7.1.1 The Solar Spectral Irradiance: Overview 349
7.1.2 Irradiance at Wavelengths Shorter Than 175 nm 350
7.1.2.1 The Lyman alpha line (121.6 nm) and its variability 350
7.1.2.2 The wavelength range 130-175 nm 351
7.1.3 A Reference Solar Spectral Irradiance for Wavelengths Longer Than 175 nm 352
7.1.3.1 The spectral region 175-210 nm 352
7.1.3.2 The spectral region 210-327.5 nm 354
7.1.3.3 The spectral region 327.5-852.5 nm 363
7.1.4 Solar Variability at Wavelengths Greater Than 175 nm 363
7.1.5 Rayleigh Scattering 367
7.1.6 Absorption by Molecular Oxygen 368
7.1.6.1 Absorption at the Lyman alpha line (121.6 nm) 368
7.1.6.2 The Schumann-Runge bands and underlying continuum 368
7.1.6.3 Absorption by the Herzberg continuum 370
7.1.7 Absorption by Ozone 375
7.1.7.1 General characteristics of ozone absorption 375
7.1.7.2 The Hartley region 375
7.1.7.3 The Huggins bands 376
7.1.7.4 The Chappuis bands 376
7.1.8 Solar Heating Rates 377

7.2 TERRESTRIAL RADIATION 378

7.2.1 Overview and Major Issues 378
7.2.2 Line-by-line Calculations, Band Transmittances, and Spectroscopic Data 380
7.2.3 Radiative Damping 382
7.2.4 Longwave Radiation in the Stratosphere 384
7.2.5 Longwave Radiation in the Mesosphere 388
7.2.6 The Distribution of Net Radiative Heating 390

7.3 CONCLUSIONS AND FUTURE RESEARCH NEEDS 391

7.0 INTRODUCTION

Solar radiation incident on the Earth and its atmosphere provides the ultimate driving force for all chemical and dynamical processes addressed in this assessment. Acting to counter the extraterrestrial energy source, longwave terrestrial radiation escapes to space thereby cooling the planet. On a globally and annually averaged basis a near balance exists between solar heating and longwave cooling. However, at any particular location and time of year a nonzero net heating, positive or negative, can exist, and this imbalance acts as a source term for the mean global circulation of the middle atmosphere. While the solar radiative heating depends only weakly on temperature, this is not true of the longwave cooling. Net radiative heating is therefore strongly influenced by the dynamical processes. In the middle atmosphere radiative and dynamical processes are inextricably coupled. Knowledge of the processes affecting both solar and terrestrial radiation is also essential for the remote sensing of middle atmosphere composition, but the emphasis of this chapter is the heat balance.

The first major subdivision of this chapter considers solar radiation and the processes that control its deposition in the Earth's atmosphere. The published data obtained since 1978 define a reference solar spectral irradiance for use in atmospheric chemical and dynamical studies, while long term satellite measurements are now providing information on variations in the Sun's output over a range of time scales. As concerns absorption of solar radiation in the atmosphere, new cross section data for molecular oxygen and ozone are now available. In the case of O_2 the revised values differ significantly from those used in atmospheric modeling at the time of WMO Report No. 11 (1982).

The second portion of this chapter addresses terrestrial longwave radiation. Major issues here relate to the accuracy of line-by-line calculations used to predict infrared flux divergences, both as regards assumptions made in radiative transfer calculations and in the spectroscopic parameters used as inputs. A valid line-by-line treatment of longwave transfer must utilize accurate line profile shapes including, for example, the temperature dependence of the half width and pressure effects on the wings. Additional topics include the influence of radiative processes on planetary scale wave activity, photochemical acceleration of radiative damping, and the breakdown of local thermodynamic equilibrium at mesospheric altitudes.

7.1 SOLAR RADIATION AND ITS ABSORPTION IN THE STRATOSPHERE AND MESOSPHERE

7.1.1 The Solar Spectral Irradiance: Overview

This section assesses the present knowledge of the solar spectral irradiance and its temporal variations at wavelengths relevant to the stratosphere and mesosphere. Since the last comprehensive NASA assessment report (WMO No. 11, 1982) and the detailed review of Simon (1981) there has been a substantial increase in the quantity of data available in the wavelength region λ = 175 to 320 nm, which is the critical portion of the spectrum for stratospheric modeling. Simon and Brasseur (1983) reviewed the information available here through the end of 1982. In addition to several rocket-borne irradiance measurements, orbiting spectrometers on the Solar Mesosphere Explorer (SME) and Nimbus 7 satellites have provided data that give an indication of irradiance variability over the 27 day solar rotation period and somewhat longer time scales. However, the state of knowledge concerning irradiance variations over the 11 year solar cycle remains inadequate, and estimates are not yet sufficiently precise. Reflecting the expanding data base, this portion of the report presents a new reference spectrum for use in stratospheric modeling. The following sections review the present knowledge of the solar irradiance, first at wavelengths less than 175 nm focusing on the Lyman alpha line and solar emission in the spectral range of the Schumann-Runge continuum. A

reference solar spectral irradiance for the region 175 to 850 nm is then presented, followed by a summary of solar variability including estimates of the magnitude of the 11 year cycle at these wavelengths.

7.1.2 Irradiance at Wavelengths Shorter than 175 nm

7.1.2.1 The Lyman Alpha Line (121.6 nm) and its Variability

Figure 7-1 illustrates the behavior of the Lyman alpha line at 121.6 nm over the 3-year period 1982-1984 as measured by the SME satellite. Values are of the integrated line emission expressed in photons $cm^{-2}s^{-1}$. The short term variations are related to the presence of active regions situated at different solar longitudes. This gives rise to periods related to the solar rotation of 27 days. The evolution of these active regions leads to irregular behavior in the amplitude of the short term variability as is evident in Figure 7-1. The straight line is a simple least squares fit to the measurements and indicates a significant decrease over the observing period corresponding to a declining level of solar activity. An estimate of the trend arising from instrument sensitivity changes has been removed from the data shown.

A change in the integrated Lyman alpha irradiance of roughly a factor of 2 over the 11 year solar cycle now has wide acceptance (Bossy and Nicolet, 1981; Lean and Skumanich, 1983). Table 7-1 lists measurements reported over the period June 1979 through July 1983 by Mount *et al.* (1980) and Mount and Rottman (1981, 1983a, 1983b, 1985) together with the 10.7 cm solar radio flux appropriate to the day of each measurement. Error bars on the two earlier flights are $\pm 15\%$ and for the latter three results

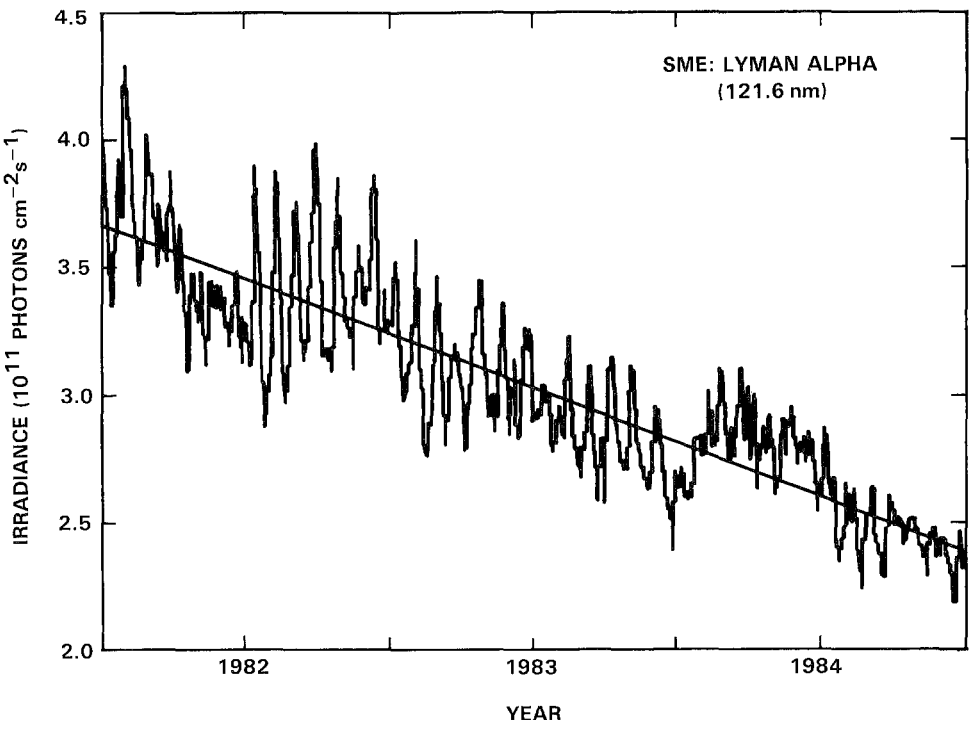

Figure 7-1. Variation in the integrated irradiance of the Lyman alpha line (121.6 nm) over the period 1982 through 1984 observed from the Solar Mesosphere Explorer satellite. The straight line is a least squares fit to the measurements. (Data provided by G.J. Rottman.)

are somewhat smaller. The factor of 2 decrease in flux from mid-1980 to mid-1983 is real. Note also that the SME measurements, extending through 1984, show Lyman alpha decreasing to values less than reported in Table 7-1. If such values are accepted, a quiet Sun value of 2.25×10^{11} photons $cm^{-2}s^{-1}$ is obtained with uncertainty limits of $\pm 15\%$. Integrated Lyman alpha flux values larger than those in Table 7-1 have appeared in the literature (Hinteregger, 1981). Although there is no obvious basis to dismiss such results, the smaller values are recommended here for use in atmospheric modeling. It is clear from a study of the experimental techniques that systematic errors can arise and great care must be taken to interpret the measurements properly (Nicolet, 1984a, 1985).

For estimates of the flux at any level of solar activity, the analytic form of Bossy and Nicolet (1981) is adequate, although the numerical constants should be altered slightly to accommodate a revised solar minimum value and the variations of Table 7-1. The recommended relationship is:

$$q(Ly\alpha) = (2.25 \times 10^{11}) + (0.014 \times 10^{11})[S_a(10.7) - 65] \quad (7.1)$$

This expression reproduces each of the values in Table 7-1 to an accuracy of $\pm 20\%$ or better. Caution is advised in accepting a simple formula as an accurate predictor of the true solar irradiance variation. Although the parameterization of Equation 7.1 predicts the gross variations in the Lyman alpha flux, the SME measurements reveal a complicated temporal variation that cannot be reproduced in detail by simple statistical relationships based on proxy solar indices. Continuing direct observations of the Lyman alpha flux, accounting for any instrumental artifacts, are required to fully define the temporal behavior.

7.1.2.2 The Wavelength Range 130-175 nm

Solar energy at wavelengths between 130 and 175 nm is deposited at altitudes above the mesopause where it dissociates molecular oxygen in the Schumann-Runge continuum. A variation in the integrated

Table 7-1. Measured Values of the Integrated Lyman Alpha Line Flux[1]

Date	Lyman Alpha Flux (photons $cm^{-2}s^{-1}$)	10.7 cm Radio Flux
June 5, 1979	5.0×10^{11}	230.2
July 15, 1980	5.5×10^{11}	218.4
May 12, 1982	3.3×10^{11}	142.2
January 12, 1983	3.0×10^{11}	135.7
July 25, 1983	2.7×10^{11}	136.7

[1]Values from Mount *et al.* (1980) and Mount and Rottman (1981, 1983a,b, 1985).

130-175 nm flux over the solar cycle of a factor of two is indicated by the rocket measurements of Table 7-2 based on Mount *et al.* (1980) and Mount and Rottman (1981, 1983a, 1985). Values reported near the last solar minimum prior to 1979, as reported in WMO No. 11 (1982), are considered less reliable than subsequent data because of improvements in calibration techniques. Error bars on the more recent results are typically $\pm 20\%$. In view of the increasing quality now obtainable, high priority should be placed on new measurements during the minimum of the present solar cycle.

Figure 7-2 presents the integrated 130-175 nm radiance derived from SME for the period 1982-1984. The percentage magnitude of the short term variation is less than that at Lyman alpha and most values lie between 7.6×10^{11} and 8.7×10^{11} photons $cm^{-2}s^{-1}$ for prevailing solar activity levels.

7.1.3 A Reference Solar Spectral Irradiance for Wavelengths Longer than 175 nm

7.1.3.1 The Spectral Region 175-210 nm

The objective of this section is to compile a reference solar spectrum for use in atmospheric modeling without regard to changes in the Sun's output over time. However, it is now universally accepted that solar irradiance in the 175 to 210 nm spectral region varies with the 27 day solar rotation period and the 11 year solar cycle (Rottman, 1983; London *et al.*, 1984; Heath and Schlesinger, 1985). At wavelengths longer than 210 nm, the threshold of the Aℓ I continuum, the percentage variability with solar rotation drops sharply as shown by the Nimbus 7 SBUV measurements of Heath *et al.* (1984). Unfortunately uncertainties in the absolute calibration of rocket-borne sensors and drifts in satellite-based instruments over long periods in orbit still inhibit definitive observations of irradiance variations over time scales of many years. To circumvent these experimental problems empirical models of solar variability have been proposed based on readily observable indices of solar activity (Cook *et al.*, 1980; Lean *et al.*, 1982; Lean, 1984) and extrapolations from observed 27 day irradiance changes to the 11 year cycle (Heath and Schlesinger, 1985).

Table 7-2. Measured Values of the Integrated Solar Irradiance Over the Wavelength Range 130-175 nm*

Date	Integrated Irradiance 130-175 nm (photons $cm^{-2}s^{-1}$)	10.7 cm Solar Radio Flux
June 5, 1979	1.5×10^{12}	230.2
July 15, 1980	1.3×10^{12}	218.4
May 17, 1982	8.0×10^{11}	142.2
July 25, 1983	7.2×10^{11}	136.7

*Values from Mount *et al.* (1980) and Mount and Rottman 1981, 1983a, 1985).

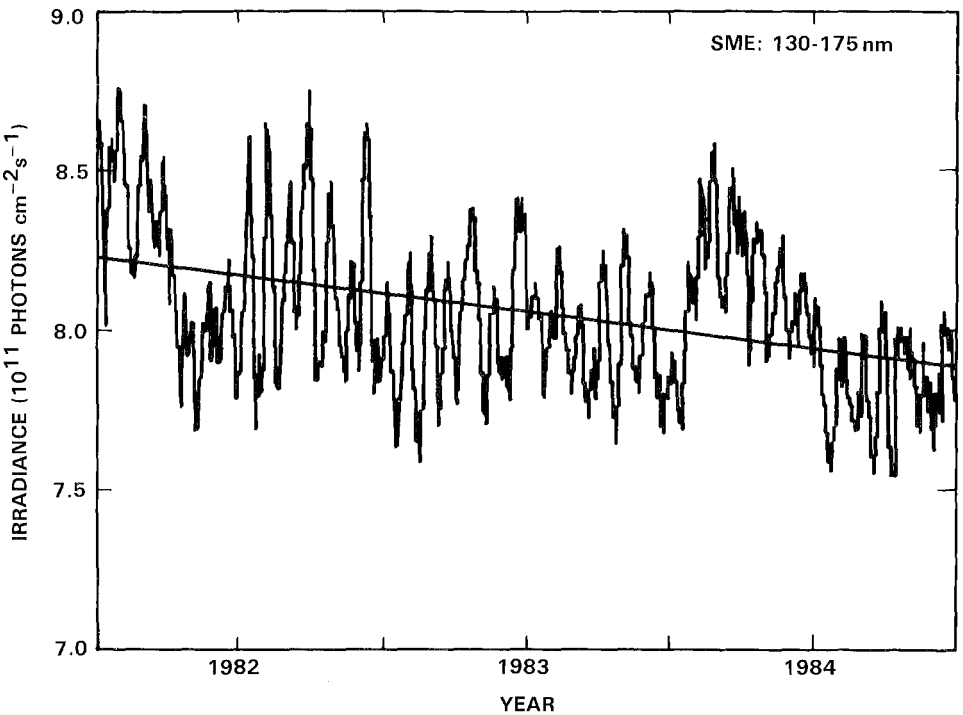

Figure 7-2. Variation in the 130-175 nm integrated irradiance over the period 1982 through 1984 observed from the Solar Mesosphere Explorer satellite. The straight line is a least squares fit to the measurements. (Data provided by G.J. Rottman.)

Table 7-3 lists the published solar irradiance measurements performed in 1978 and later. Also given are the 10.7 cm solar radio flux, $S_a(10.7)$, adjusted to one astronomical unit for the day of each measurement. Data obtained prior to 1978 have been discussed by Simon (1981) and in WMO No. 11 (1982). Examination of the data corresponding to the entries of Table 7-3 shows no clear relationship between absolute irradiance and the solar activity indices. This certainly reflects experimental uncertainties rather than the absence of a solar cycle dependence since the theoretical basis for irradiance variations is firm. Given no definitive information showing that one measurement is superior to another, the best estimate for a reference solar irradiance in a given spectral interval is the mean of all available data. However, if one measurement is known to be deficient in some respect, it is acceptable to eliminate this data set when compiling the final spectrum. The approach used to define the reference spectrum is therefore as follows: All data corresponding to the entries of Table 7-3 were placed on the 500 cm^{-1} wavenumber grid that has become standard in atmospheric modeling since its first use by Ackerman (1971). The mean of all available data was then computed. The final reference spectrum in Table 7-4 is denoted by $F_{REF}(i)$ where the spectral intervals $i = 1,2,\ldots,19$ correspond to wavelengths from 175.439 to 210.526 nm. In generating the spectrum, the data of June 5, 1979 were eliminated for wavelengths longer than 180 nm as recommended by G.H. Mount. A useful index of the scatter in the available data is the root mean square (RMS) deviation from the mean reference spectrum. For spectral intervals i_1 to i_2 this is defined as:

$$\epsilon(i_1,i_2) = 100\left[\frac{1}{(i_2-i_1+1)}\sum_{i=i_1}^{i_2}\left\{\frac{F(i)-F_{REF}(i)}{F_{REF}(i)}\right\}^2\right]^{1/2}$$

Here F(i) is the irradiance in interval i from a data source listed in Table 7-3 and $F_{REF}(i)$ is the mean of all acceptable measurements. Table 7-3 includes the computed RMS deviations for $(i_1,i_2) = (1,19)$. In most cases these values are less than 10% although the quoted uncertainty in any single measurement is typically $\pm 15\%$-20%. The mean 10.7 cm radio flux for all measurements entering the final reference spectrum is approximately 185, corresponding to a moderate level of solar activity.

7.1.3.2 The Spectral Region 210-327.5 nm

The solar irradiance in the spectral region 210-330 nm is responsible for dissociating ozone and other trace gases significant in the photochemistry of the stratosphere and mesosphere. In addition, photons at wavelengths up to 240 nm dissociate molecular oxygen via the Herzberg continuum. The data available to define the absolute solar spectral irradiance in this wavelength range were sparse for many years, the single comprehensive spectrum being Broadfoot (1972) derived from a rocket measurement made on June 15, 1970. Simon (1981) has presented a detailed discussion of data available as of 1980. The only measurements that spanned the entire wavelength region 210-330 nm at that time were by Broadfoot (1972) and Heath (1980), although several other data sets covered portions of this interval (Simon, 1975; Mount *et al.*, 1980; Simon *et al.*, 1982; Arvesen *et al.*, 1969). Since Simon's (1981) review a significant number of

Table 7-3. Solar Spectral Irradiance Measurements for Wavelengths 175.439 – 210.526 nm Considered in Developing the Reference Spectrum*

Date of Measurement	S_a(10.7 cm) Radio Flux	RMS Deviation $\epsilon(1,19)$%	Reference
Nov. 7, 1978	174.6	9.6	Heath (1980)
Nov. 16, 1978	128.8	7.8	Mentall *et al.* (1985)
June 5, 1979[1]	230.2	14.2	Mount *et al.* (1980)
May 22, 1980	276.6	11.4	Mentall *et al.* (1985)
July 15, 1980	218.4	6.5	Mount and Rottman (1981)
Sept. 15, 1980	153.8	7.8	Mentall *et al.* (1981)
Oct. 16, 1981	302.4	11.9	Mentall *et al.* (1985)
May 17, 1982	142.2	4.6	Mount and Rottman (1983a)
Jan. 12, 1983	135.7	6.2	Mount and Rottman (1983b)
July 25, 1983	136.7	7.2	Mount and Rottman (1985)

*Data from this measurement at wavelengths greater than 180 nm were not included in computing the final reference spectrum of Table 6-4.

rocket-borne measurements that very nearly cover the entire 210-330 nm wavelength range have been reported in the literature. The present assessment focuses on measurements made in the years 1978 and later. This limited scope reflects the belief that improvements in measurement techniques make the more recent results preferable to early data and that sufficient data exist in the 1978-1984 time frame to assemble a useful reference spectrum for atmospheric modeling irrespective of the earlier results. Table 7-5 lists the measurements considered here. The accuracy of the irradiance values derived by Mount and Rottman (1981, 1983a,b, 1985) degrades at wavelengths above 296 nm, and results beyond this limit were therefore excluded from the average. Typical uncertainty limits including both systematic and random errors are ±15-20%. The RMS deviations from the reference spectrum, $\epsilon(i=20, 53)$ as defined in Equation 7.2, for all data sets listed in Table 7-5 were less than 10%. The systematic differences between the results of Mount and Rottman (1981, 1983a,b, 1985), Heath (1980), and Mentall *et al.* (1981) are 5-10%. The results are given as the reference spectrum in Table 7-4 for spectral intervals i=20 to 53.

Table 7-4. Reference Solar Irradiance, Rayleigh Scattering, O_2 and O_3 Cross Sections

Spectral Interval	Wavelength* Range (nm)	Irradiance (Photons $cm^{-2}s^{-1}$)	Ray. Scat. $\sigma_{RS}(cm^2)$	O_2 Herzberg $\sigma_{HZ}(O_2)$ (cm^2)	Ozone $\sigma(O_3)$ (cm^2) T=203K	Ozone $\sigma(O_3)$ (cm^2) T=273K
1	175.439 - 176.991	1.74E+11	6.79E−25	4.61E−24	8.11E−19	
2	176.991 - 178.571	2.10E+11	6.49E−25	5.03E−24	7.99E−19	
3	178.571 - 180.180	2.38E+11	6.20E−25	5.46E−24	7.86E−19	
4	180.180 - 181.818	3.04E+11	5.93E−25	5.88E−24	7.63E−19	
5	181.818 - 183.486	3.19E+11	5.66E−25	6.29E−24	7.29E−19	
6	183.486 - 185.185	2.93E+11	5.41E−25	6.68E−24	6.88E−19	
7	185.185 - 186.916	3.62E+11	5.16E−25	7.04E−24	6.40E−19	
8	186.916 - 188.679	4.73E+11	4.93E−25	7.36E−24	5.88E−19	
9	188.679 - 190.476	5.61E+11	4.70E−25	7.64E−24	5.31E−19	
10	190.476 - 192.308	6.63E+11	4.49E−25	7.87E−24	4.80E−19	
11	192.308 - 194.175	6.90E+11	4.28E−25	8.04E−24	4.38E−19	
12	194.175 - 196.078	9.56E+11	4.08E−25	8.14E−24	4.11E−19	
13	196.078 - 198.020	1.15E+12	3.89E−25	8.17E−24	3.69E−19	
14	198.020 - 200.000	1.27E+12	3.71E−25	8.13E−24	3.30E−19	

Table 7-4. Reference Solar Irradiance, Rayleigh Scattering, O_2 and O_3 Cross Sections (Continued)

Spectral Interval	Wavelength* Range (nm)	Irradiance (Photons $cm^{-2}s^{-1}$)	Ray. Scat. $\sigma_{RS}(cm^2)$	O_2 Herzberg $\sigma_{HZ}(O_2)$ (cm^2)	Ozone $\sigma(O_3)$ (cm^2) T=203K	Ozone $\sigma(O_3)$ (cm^2) T=273K
15	200.000 - 202.020	1.52E+12	3.53E−25	8.01E−24	3.26E−19	
16	202.020 - 204.082	1.78E+12	3.36E−25	7.84E−24	3.26E−19	
17	204.082 - 206.186	2.20E+12	3.20E−25	7.63E−24	3.51E−19	
18	206.186 - 208.333	2.69E+12	3.05E−25	7.33E−24	4.11E−19	
19	208.333 - 210.526	4.54E+12	2.90E−25	6.99E−24	4.84E−19	
20	210.526 - 212.766	7.14E+12	2.76E−25	6.45E−24	6.26E−19	
21	212.766 - 215.054	8.35E+12	2.62E−25	5.81E−24	8.57E−19	
22	215.054 - 217.391	8.39E+12	2.49E−25	5.23E−24	1.17E−18	
23	217.391 - 219.780	1.08E+13	2.36E−25	4.71E−24	1.52E−18	
24	219.780 - 222.222	1.18E+13	2.24E−25	4.26E−24	1.97E−18	
25	222.222 - 224.719	1.60E+13	2.13E−25	3.80E−24	2.55E−18	
26	224.719 - 227.273	1.34E+13	2.02E−25	3.35E−24	3.24E−18	
27	227.273 - 229.885	1.41E+13	1.92E−25	2.90E−24	4.00E−18	
28	229.885 - 232.558	1.57E+13	1.82E−25	2.45E−24	4.83E−18	
29	232.558 - 235.294	1.38E+13	1.72E−25	2.05E−24	5.79E−18	
30	235.294 - 238.095	1.60E+13	1.63E−25	1.69E−24	6.86E−18	
31	238.095 - 240.964	1.45E+13	1.54E−25	1.30E−24	7.97E−18	
32	240.964 - 243.902	2.20E+13	1.46E−25	0.93E−24	9.00E−18	
33	243.902 - 246.914	1.99E+13	1.38E−25	0.00E−00	1.00E−17	
34	246.914 - 250.000	1.97E+13	1.31E−25		1.08E−17	
35	250.000 - 253.165	1.94E+13	1.23E−25		1.13E−17	

Table 7-4. Reference Solar Irradiance, Rayleigh Scattering, O_2 and O_3 Cross Sections (Continued)

Spectral Interval	Wavelength* Range (nm)	Irradiance (Photons $cm^{-2}s^{-1}$)	Ray. Scat. $\sigma_{RS}(cm^2)$	O_2 Herzberg $\sigma_{HZ}(O_2)$ (cm^2)	Ozone $\sigma(O_3)$ (cm^2) T=203K	Ozone $\sigma(O_3)$ (cm^2) T=273K
36	253.165 - 256.410	2.91E+13	1.17E−25		1.15E−17	
37	256.410 - 259.740	4.95E+13	1.10E−25		1.12E−17	
38	259.740 - 263.158	4.53E+13	1.04E−25		1.06E−17	
39	263.158 - 266.667	1.07E+14	9.78E−26		9.59E−18	9.65E−18
40	266.667 - 270.270	1.20E+14	9.22E−26		8.31E−18	8.34E−18
41	270.270 - 273.973	1.10E+14	8.68E−26		6.89E−18	6.92E−18
42	273.973 - 277.778	1.04E+14	8.17E−26		5.35E−18	5.42E−18
43	277.778 - 281.690	8.24E+13	7.68E−26		3.91E−18	4.02E−18
44	281.690 - 285.714	1.52E+14	7.22E−26		2.67E−18	2.77E−18
45	285.714 - 289.855	2.15E+14	6.78E−26		1.73E−18	1.79E−18
46	289.855 - 294.118	3.48E+14	6.36E−26		1.04E−18	1.09E−18
47	294.118 - 298.507	3.40E+14	5.97E−26		5.85E−19	6.24E−19
48	298.507 - 303.030	3.22E+14	5.59E−26		3.16E−19	3.43E−19
49	303.030 - 307.692	4.23E+14	5.24E−26		1.66E−19	1.85E−19
50	307.692 - 312.5	4.95E+14	4.90E−26		8.67E−20	9.80E−20
51	312.5 - 317.5	5.44E+14	4.58E−26		4.33E−20	5.01E−20
52	317.5 - 322.5	5.93E+14	4.28E−26		2.09E−20	2.49E−20
53	322.5 - 327.5	6.95E+14	4.01E−26		9.37E−21	1.20E−20
54	327.5 - 332.5	8.15E+14	3.75E−26		4.71E−21	6.17E−21
55	332.5 - 337.5	7.81E+14	3.52E−26		1.98E−21	2.74E−21
56	337.5 - 342.5	8.35E+14	3.31E−26		7.77E−22	1.17E−21

Table 7-4. Reference Solar Irradiance, Rayleigh Scattering, O_2 and O_3 Cross Sections (Continued)

Spectral Interval	Wavelength* Range (nm)	Irradiance (Photons $cm^{-2}s^{-1}$)	Ray. Scat. $\sigma_{RS}(cm^2)$	Ozone $\sigma(O_3)$ (cm^2) T=203K	Ozone $\sigma(O_3)$ (cm^2) T=273K
57	342.5 - 347.5	8.14E+14	3.11E−26	1.77E−22	5.88E−22
58	347.5 - 352.5	8.53E+14	2.92E−26	—	2.66E−22
59	352.5 - 357.5	9.17E+14	2.75E−26	—	1.09E−22
60	357.5 - 362.5	8.38E+14	2.60E−26	—	5.49E−23
61	362.5 - 367.5	1.04E+15	2.45E−26	—	—
62	367.5 - 372.5	1.10E+15	2.31E−26	—	—
63	372.5 - 377.5	9.79E+14	2.19E−26	—	—
64	377.5 - 382.5	1.13E+15	2.07E−26	—	—
65	382.5 - 387.5	8.89E+14	1.96E−26	—	—
66	387.5 - 392.5	1.14E+15	1.86E−26	—	—
67	392.5 - 397.5	9.17E+14	1.76E−26	—	—
68	397.5 - 402.5	1.69E+15	1.67E−26	—	—
69	402.5 - 407.5	1.70E+15	1.59E−26	—	—
70	407.5 - 412.5	1.84E+15	1.51E−26	2.91E−23	
71	412.5 - 417.5	1.87E+15	1.44E−26	3.14E−23	
72	417.5 - 422.5	1.95E+15	1.37E−26	3.99E−23	
73	422.5 - 427.5	1.81E+15	1.30E−26	6.54E−23	
74	427.5 - 432.5	1.67E+15	1.24E−26	6.83E−23	
75	432.5 - 437.5	1.98E+15	1.18E−26	8.66E−23	
76	437.5 - 442.5	2.02E+15	1.13E−26	1.25E−22	
77	442.5 - 447.5	2.18E+15	1.08E−26	1.49E−22	

Table 7-4. Reference Solar Irradiance, Rayleigh Scattering, O_2 and O_3 Cross Sections (Continued)

Spectral Interval	Wavelength* Range (nm)	Irradiance (Photons $cm^{-2}s^{-1}$)	Ray. Scat. $\sigma_{RS}(cm^2)$	O_2 Herzberg $\sigma_{HZ}(O_2)$ (cm^2)	Ozone $\sigma(O_3)$ (cm^2) T=203K	Ozone $\sigma(O_3)$ (cm^2) T=273K
78	447.5 - 452.5	2.36E+15	1.03E−26		1.71E−22	
79	452.5 - 457.5	2.31E+15	9.85E−27		2.12E−22	
80	457.5 - 462.5	2.39E+15	9.42E−27		3.57E−22	
81	462.5 - 467.5	2.38E+15	9.01E−27		3.68E−22	
82	467.5 - 472.5	2.39E+15	8.63E−27		4.06E−22	
83	472.5 - 477.5	2.44E+15	8.26E−27		4.89E−22	
84	477.5 - 482.5	2.51E+15	7.92E−27		7.11E−22	
85	482.5 - 487.5	2.30E+15	7.59E−27		8.43E−22	
86	487.5 - 492.5	2.39E+15	7.28E−27		8.28E−22	
87	492.5 - 497.5	2.48E+15	6.99E−27		9.09E−22	
88	497.5 - 502.5	2.40E+15	6.71E−27		1.22E−21	
89	502.5 - 507.5	2.46E+15	6.44E−27		1.62E−21	
90	507.5 - 512.5	2.49E+15	6.19E−27		1.58E−21	
91	512.5 - 517.5	2.32E+15	5.95E−27		1.60E−21	
92	517.5 - 522.5	2.39E+15	5.72E−27		1.78E−21	
93	522.5 - 527.5	2.42E+15	5.50E−27		2.07E−21	
94	527.5 - 532.5	2.55E+15	5.30E−27		2.55E−21	
95	532.5 - 537.5	2.51E+15	5.10E−27		2.74E−21	
96	537.5 - 542.5	2.49E+15	4.91E−27		2.88E−21	
97	542.5 - 547.5	2.55E+15	4.73E−27		3.07E−21	
98	547.5 - 552.5	2.53E+15	4.56E−27		3.17E−21	

Table 7-4. Reference Solar Irradiance, Rayleigh Scattering, O_2 and O_3 Cross Sections (Continued)

Spectral Interval	Wavelength* Range (nm)	Irradiance (Photons $cm^{-2}s^{-1}$)	Ray. Scat. $\sigma_{RS}(cm^2)$	Ozone $\sigma(O_3)$ (cm^2) T=203K	Ozone $\sigma(O_3)$ (cm^2) T=273K
99	552.5 - 557.5	2.54E+15	4.34E−27		3.36E−21
100	557.5 - 562.5	2.50E+15	4.18E−27		3.88E−21
101	562.5 - 567.5	2.57E+15	4.04E−27		4.31E−21
102	567.5 - 572.5	2.58E+15	3.90E−27		4.67E−21
103	572.5 - 577.5	2.67E+15	3.76E−27		4.75E−21
104	577.5 - 582.5	2.67E+15	3.63E−27		4.55E−21
105	582.5 - 587.5	2.70E+15	3.51E−27		4.35E−21
106	587.5 - 592.5	2.62E+15	3.39E−27		4.42E−21
107	592.5 - 597.5	2.69E+15	3.28E−27		4.61E−21
108	597.5 - 602.5	2.63E+15	3.17E−27		4.89E−21
109	602.5 - 607.5	2.68E+15	3.06E−27		4.84E−21
110	607.5 - 612.5	2.66E+15	2.96E−27		4.54E−21
111	612.5 - 617.5	2.59E+15	2.87E−27		4.24E−21
112	617.5 - 622.5	2.69E+15	2.77E−27		3.90E−21
113	622.5 - 627.5	2.61E+15	2.68E−27		3.60E−21
114	627.5 - 632.5	2.62E+15	2.60E−27		3.43E−21
115	632.5 - 637.5	2.62E+15	2.52E−27		3.17E−21
116	637.5 - 642.5	2.63E+15	2.44E−27		2.74E−21
117	642.5 - 647.5	2.60E+15	2.36E−27		2.61E−21
118	647.5 - 652.5	2.55E+15	2.29E−27		2.42E−21
119	652.5 - 657.5	2.48E+15	2.22E−27		2.20E−21

Table 7-4. Reference Solar Irradiance, Rayleigh Scattering, O_2 and O_3 Cross Sections (Continued)

Spectral Interval	Wavelength* Range (nm)	Irradiance (Photons $cm^{-2}s^{-1}$)	Ray. Scat. $\sigma_{RS}(cm^2)$	Ozone $\sigma(O_3)$ (cm^2) T=203K	Ozone $\sigma(O_3)$ (cm^2) T=273K
120	657.5 - 662.5	2.57E+15	2.15E−27		2.02E−21
121	662.5 - 667.5	2.61E+15	2.09E−27		1.85E−21
122	667.5 - 672.5	2.61E+15	2.03E−27		1.67E−21
123	672.5 - 677.5	2.62E+15	1.97E−27		1.54E−21
124	677.5 - 682.5	2.62E+15	1.91E−27		1.42E−21
125	682.5 - 687.5	2.57E+15	1.85E−27		1.25E−21
126	687.5 - 692.5	2.52E+15	1.80E−27		1.12E−21
127	692.5 - 697.5	2.60E+15	1.75E−27		1.02E−21
128	697.5 - 702.5	2.58E+15	1.70E−27		9.20E−22
129	702.5 - 707.5	2.52E+15	1.65E−27		8.40E−22
130	707.5 - 712.5	2.51E+15	1.60E−27		7.70E−22
131	712.5 - 717.5	2.48E+15	1.56E−27		6.90E−22
132	717.5 - 722.5	2.45E+15	1.52E−27		6.30E−22
133	722.5 - 727.5	2.48E+15	1.47E−27		5.70E−22
134	727.5 - 732.5	2.45E+15	1.43E−27		5.25E−22
135	732.5 - 737.5	2.44E+15	1.39E−27		4.75E−22
136	737.5 - 742.5	2.39E+15	1.36E−27		4.47E−22
137	742.5 - 747.5	2.40E+15	1.32E−27		4.20E−22
138	747.5 - 752.5	2.41E+15	1.29E−27		3.75E−22
139	752.5 - 757.5	2.40E+15	1.25E−27		3.25E−22
140	757.5 - 762.5	2.38E+15	1.22E−27		2.92E−22

Table 7-4. Reference Solar Irradiance, Rayleigh Scattering, O_2 and O_3 Cross Sections (Continued)

Spectral Interval	Wavelength* Range (nm)	Irradiance (Photons $cm^{-2}s^{-1}$)	Ray. Scat. $\sigma_{RS}(cm^2)$	Ozone $\sigma(O_3)$ (cm^2) T=203K	Ozone $\sigma(O_3)$ (cm^2) T=273K
141	762.5 - 767.5	2.34E+15	1.19E−27		2.76E−22
142	767.5 - 772.5	2.32E+15	1.16E−27		2.70E−22
143	772.5 - 777.5	2.30E+15	1.13E−27		2.80E−22
144	777.5 - 782.5	2.33E+15	1.10E−27		2.85E−22
145	782.5 - 787.5	2.34E+15	1.07E−27		2.52E−22
146	787.5 - 792.5	2.29E+15	1.04E−27		2.20E−22
147	792.5 - 797.5	2.29E+15	1.02E−27		1.82E−22
148	797.5 - 802.5	2.27E+15	9.90E−28		1.63E−22
149	802.5 - 807.5	2.27E+15	9.66E−28		1.75E−22
150	807.5 - 812.5	2.20E+15	9.42E−28		1.90E−22
151	812.5 - 817.5	2.22E+15	9.19E−28		1.85E−22
152	817.5 - 822.5	2.18E+15	8.96E−28		1.70E−22
153	822.5 - 827.5	2.20E+15	8.75E−28		1.52E−22
154	827.5 - 832.5	2.14E+15	8.53E−28		1.42E−22
155	832.5 - 837.5	2.14E+15	8.33E−28		1.40E−22
156	837.5 - 842.5	2.13E+15	8.13E−28		1.40E−22
157	842.5 - 847.5	2.09E+15	7.94E−28		1.42E−22
158	847.5 - 852.5	2.05E+15	7.75E−28		1.45E−22

* Wavelength range for spectral intervals 1-49 correspond to 500 wavenumbers. Wavelength range for remainder of spectral intervals is 5 nm.

Table 7-5. Solar Spectral Irradiance Measurements for Wavelengths 210.526 – 327.5 nm Considered in Developing the Reference Spectrum

Date of Measurement	RMS Deviation $\epsilon(20,53)\%$	Reference
Nov. 7, 1978	3.3	Heath (1980)
July 15, 1980	5.3	Mount and Rottman (1981)[1]
Sept. 15, 1980	6.2	Mentall *et al.* (1981)
May 17, 1982	3.1	Mount and Rottman (1983a)[1]
Jan. 12, 1983	3.0	Mount and Rottman (1983b)[1]
July 25, 1983	3.3	Mount and Rottman (1985)[1]

[1]Values at wavelengths greater than 296 nm were excluded in compiling the reference spectrum.

7.1.3.3 The Spectral Region 327.5 - 852.5 nm

Recommended values of the solar irradiance at wavelengths greater than 327.5 nm have not changed significantly since the comprehensive review of Nicolet (1981) and WMO No. 11 (1982). The available data sets here are the Nimbus 7 SBUV results of Heath (1980) extending to 400 nm and the results of Arvesen *et al.* (1969) and Neckel and Labs (1984). The values in Table 7-4 from 327.5 to 397.5 nm (i = 54 to 67) are based on Heath (1980) and at longer wavelengths are the same as given in WMO No. 11 (1982) which includes a discussion of the uncertainties. In the visible the accuracy is $\pm 3\%$, but this degrades somewhat toward the ultraviolet.

7.1.4 Solar Variability at Wavelengths Greater than 175 nm

Figure 7-3 illustrates the variation in irradiance received at the Earth as a function of wavelength over two 27 day solar rotation periods in November/December 1979 and August/September 1980 as observed by the Nimbus 7 SBUV instrument (Heath *et al.*, 1984). Between 175 and 210 nm, the spectral region important for production of atmospheric odd oxygen, the maximum irradiance during the December 1979 rotation tends to be 1.05 to 1.07 times the minimum value with a peak ratio approaching 1.10. The Aℓ I edge near 210 nm is an obvious feature longward of which the fractional variations decrease markedly. Between 210 and 250 nm the maximum to minimum irradiance ratio is typically 1.03 and beyond 260 nm drops to 1.01 or less. An exception is the large variation in the core of the Mg II absorption feature near 280 nm. The changes observed during the September rotation are much less pronounced. Figures 7-4, 7-5, and 7-6 for the wavelength regions 175-195 nm, 195-208 nm, and 240-260 nm respectively show that the variability of the irradiance is not exactly repeatable from one solar rotation to another, as would be expected from the evolution of active regions.

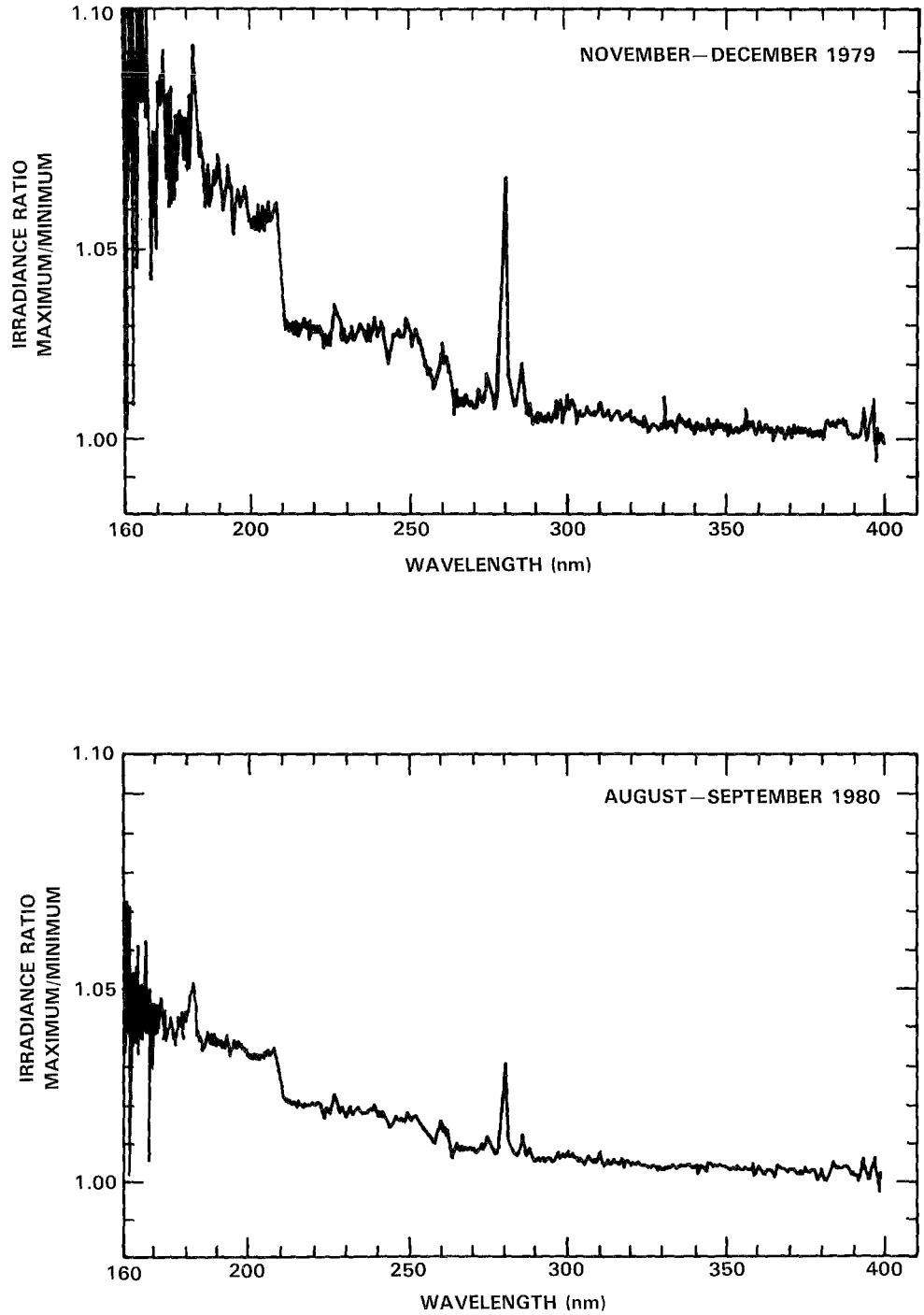

Figure 7-3. Variation in the solar irradiance over two 27 day rotation periods in November-December 1979 and August-September 1980. The ratio is of the maximum irradiance observed during the rotation to the mean of the preceding and following minima. Values are from the Nimbus 7 SBUV experiment (Heath *et al.*, 1984).

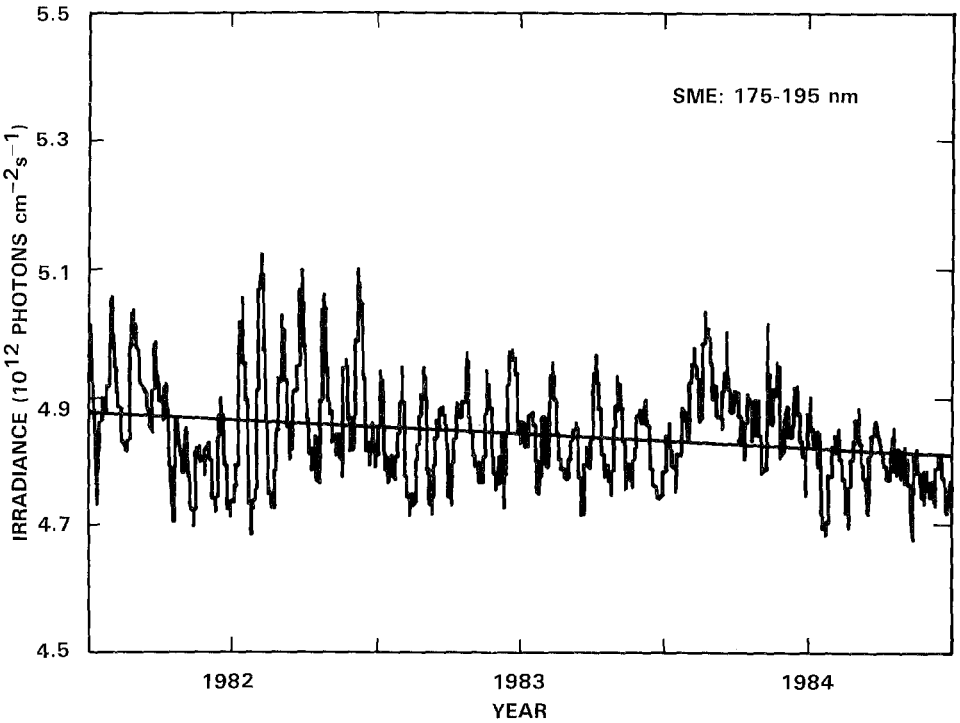

Figure 7-4. Variation in the 175-195 nm integrated irradiance over the period 1982 through 1984 observed from the Solar Mesosphere Explorer satellite. The straight line is a least squares fit to the measurements. (Data provided by G.J. Rottman.)

A linear fit to the values in Figures 7-4 through 7-6 and extrapolation provides a rough measure of solar variations over time scales of years. Table 7-6 presents estimates of the solar cycle variability in selected wavelength bins spanning the region 175 to 300 nm. The reported quantity, R_{sc}, is a measure of the ratio of solar maximum irradiance to solar minimum irradiance obtained from a linear fit to all of the SME measurements. The uncertainty limits account for possible instrument drifts that may still influence the results after a correction for this has been applied. Caution is advised in a physical interpretation of the R_{sc} values. The tabulated results give the ratio of a typical irradiance averaged over a 27 day rotation period at solar maximum to the same average performed at solar minimum. Also included in Table 7-6 is an estimate of the 27 day irradiance variation, R_{27}, from the data of Figure 7-3. If this is taken as a typical mean solar rotation, then the ratio of maximum to minimum irradiance during a solar cycle is the product $R_{27}R_{sc}$. For model calculations of atmospheric response to an 11 year solar variability, the maximum and minimum irradiances, $F_{MAX}(i)$ and $F_{MIN}(i)$, are related to the mean reference spectrum of Table 7-4 by:

$$F_{MAX}(i) = F_{REF}(i) \left[\frac{2\ R_{27}(i)\ R_{sc}(i)}{1 + R_{27}(i)\ R_{sc}(i)} \right] \tag{7.3}$$

and

$$F_{MIN}(i) = F_{REF}(i) \left[\frac{2}{1 + R_{27}(i)\ R_{sc}(i)} \right] \tag{7.4}$$

where $R_{27}(i)$ and $R_{sc}(i)$ must be derived for each spectral interval based on Table 7-6.

Table 7-6. Parameters for Estimating Irradiance Variability over the 11 Year Solar Cycle

Wavelength Range	R^1_{sc} (max/min)	R^2_{27} (max/min)
175 - 190	1.020 (±0.020)	1.07
190 - 210	1.030 (±0.020)	1.06
210 - 240	1.026 (±0.020)	1.03
240 - 300	1.005 (±0.020)	1.01

[1] R_{sc} is the ratio of a 27 day mean irradiance near solar maximum to a 27 day mean at solar minimum.
[2] R_{27} is the ratio of the maximum irradiance observed during a typical 27 day solar rotation to the minimum irradiance during this rotation.

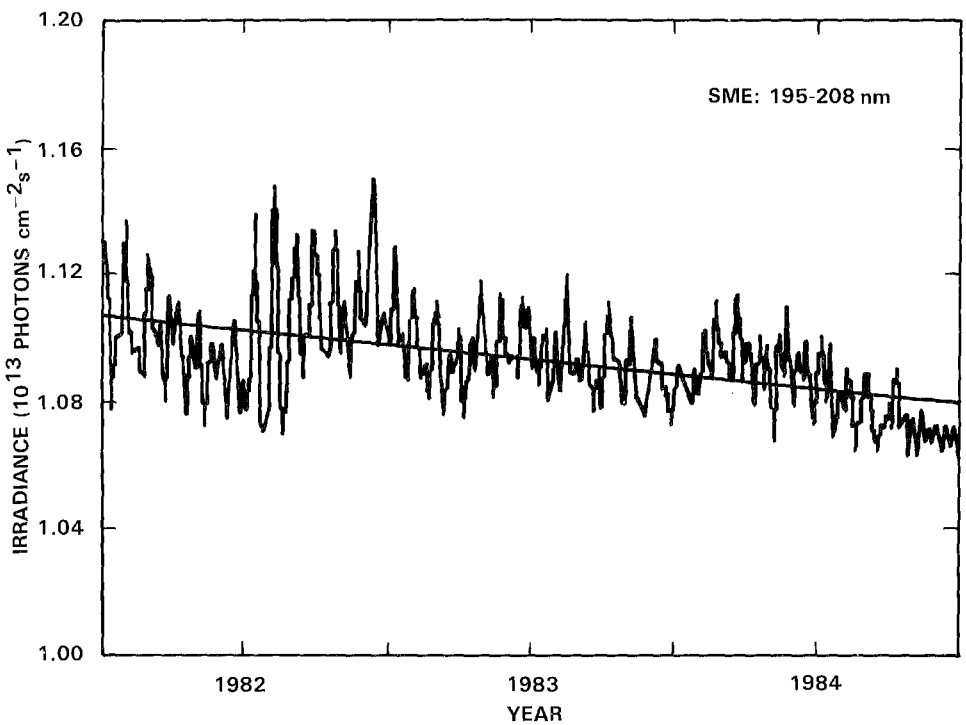

Figure 7-5. Variation in the 195-208 nm integrated irradiance over the period 1982 through 1984 observed from the Solar Mesosphere Explorer satellite. The straight line is a least squares fit to the measurements. (Data provided by G.J. Rottman.)

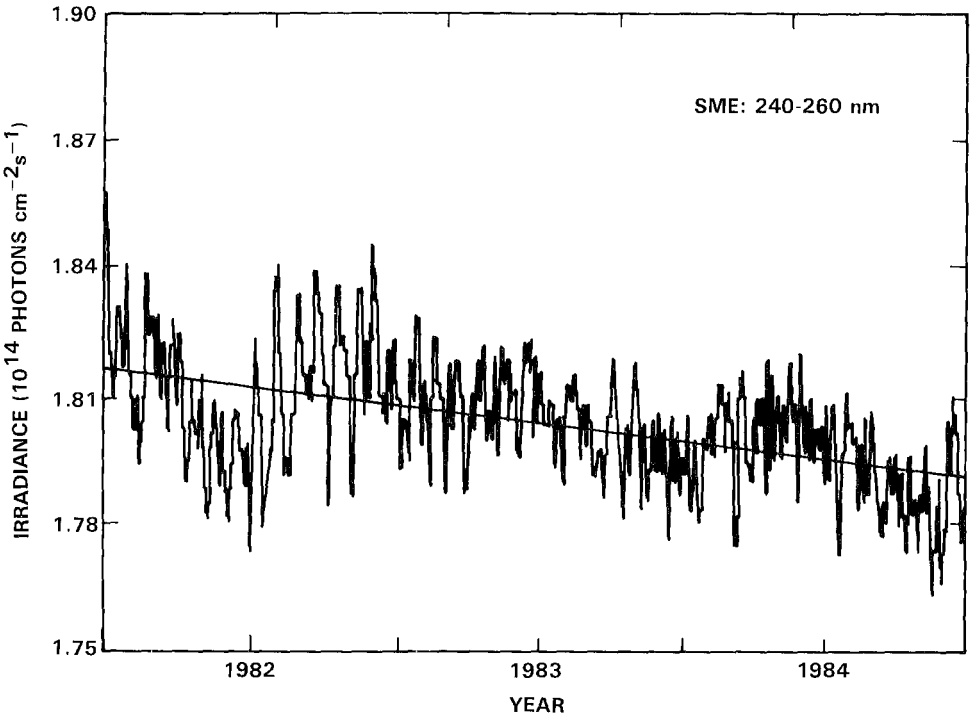

Figure 7-6. Variation in the 240-260 nm integrated irradiance over the period 1982 through 1984 observed from the Solar Mesosphere Explorer satellite. The straight line is a least squares fit to the measurements. (Data provided by G.J Rottman.)

It must be recognized that any estimate of solar cycle variability based on the available measurements contains a large uncertainty, and the recommendations given above will surely change as more information becomes available. Estimates of solar variability from Table 7-6 are much smaller than recent predictions derived from empirical models of solar activity. The model of Lean (1984) uses Nimbus 7 SBUV observations of short term irradiance changes and from this infers the behavior over an 11 year cycle. This procedure predicts a 25% minimum to maximum variation at 200 nm, decreasing to 10% between 210 and 250 nm. As the long term data base increases, further empirical modeling to relate observed irradiance behavior to readily measured indices of solar activity is strongly encouraged. However, in view of the complex behavior displayed by the solar irradiance, the major emphasis must be on the acquisition of a long term data base that is essentially free of instrumental artifacts.

7.1.5 Rayleigh Scattering

An accurate calculation of the solar radiation field reaching the lower stratosphere and troposphere at wavelengths greater than 290 nm requires inclusion of multiple Rayleigh scattering and reflection from the lower boundary, particularly cloud decks (Meier *et al.*, 1982; Nicolet *et al.*, 1982). In addition, at wavelengths near 210 nm the optical depth for Rayleigh scattering is approximately 20% of that associated with the Herzberg continuum of O_2. Recently Bates (1984) re-evaluated the cross section for Rayleigh scattering in air and using these results Nicolet (1984a) has derived analytic expressions for use in aeronomic calculations. With wavelength λ expressed in microns the following formula applies:

$$\sigma_{RS}(\lambda) = \frac{4.02\times10^{-28}}{\lambda^{4+\chi}} \tag{7.5}$$

where $\sigma_{RS}(\lambda)$ is the Rayleigh scattering cross section in cm^2 and the parameter χ is given by:

$$\chi = 0.389\lambda + \frac{0.09426}{\lambda} - 0.3228 \tag{7.6}$$

for $0.20\mu \leq \lambda \leq 0.55\mu$ and:

$$\chi = 0.04 \tag{7.7}$$

for $0.55\mu < \lambda \leq 1.0\mu$. Nicolet (1984) notes that Equations 7.5 and 7.6 produce accurate results at least to a wavelength of 0.190μ. Table 7-4 includes values of the Rayleigh scattering cross section for use in atmospheric modeling.

7.1.6 Absorption by Molecular Oxygen

7.1.6.1 Absorption at the Lyman Alpha Line (121.6 nm)

Absorption by O_2 controls the penetration of the H Lyman alpha line into the mesosphere. The primary complication involved in treating the transfer of this radiation concerns the need to convolve the Lyman alpha self-reversed profile with the O_2 absorption cross section, which varies significantly over an interval of ± 0.1 nm about line center (Frederick and Hudson 1980a; Lewis *et al.*, 1983; Nicolet, 1985). Early laboratory measurements showed the O_2 cross section to vary in the range 1×10^{-20} to $3\times10^{-20}cm^2$ over the line profile (Ogawa, 1971) and more recent data have defined the temperature dependence (Carver *et al.*, 1977). The change in profile shape with optical depth can be incorporated into transmission calculations by use of an effective cross section which depends on O_2 column content, N, measured along the path of the solar beam. For a temperature of 230K Nicolet (1985) derived the expression

$$T(Ly\alpha) = \exp[-2.115\times10^{-18}\ N^{0.8855}] \tag{7.8}$$

where T is the Lyman alpha transmission and N is in cm^{-2}. The effective O_2 cross section is $\sigma_{eff} = 2.115\times10^{-18}\ N^{-0.1145}$. For $N = 1\times10^{20}cm^{-2}$ this gives $\sigma_{eff} = 1.08\times10^{-20}cm^2$ which is close to the laboratory measurements. Equation 7.8 is recommended for use in atmospheric calculations.

7.1.6.2 The Schumann-Runge Bands and Underlying Continuum

At wavelengths shortward of 205 nm extending to 175 nm the Schumann-Runge bands of molecular oxygen are a major absorption feature, corresponding to the transition $B^3\Sigma_u^- \leftarrow X^3\Sigma_g^-$. Predissociation yielding two $O(^3P)$ atoms occurs via one or more repulsive states in more that 99% of the absorptions (Hudson and Mahle, 1972). Because a predissociation is involved, the cross section consists of thousands of individual rotational lines. The Schumann-Runge band absorption is generally viewed as the dominant source of atmospheric odd oxygen at altitudes greater than 60 km; however, this transition is significant at stratospheric altitudes for a different reason. At discrete wavelengths situated in between the rotational peaks the cross section drops to small values ($\sim 10^{-24} - 10^{-23}$ cm^2) and solar radiation at these selected

wavelengths, particularly above 190 nm, can then penetrate into the middle stratosphere. Several source molecules, such as nitrous oxide and the chlorofluorocarbons, have large cross sections in the 175-200 nm spectral region and significant fractions of their total dissociation rates arise from absorption here. Hence, in modeling the Schumann-Runge band system it is critical to consider details of the line shapes since the overlapping wings of thousands of lines sum to form the smooth pseudo-continuum cross section located between the rotational peaks.

The Schumann-Runge bands are not the only transition that contributes to the total O_2 dissociation cross section between 175 and 205 nm. The Herzberg continuum extends throughout this spectral region, while absorption by excited vibrational levels in the Schumann-Runge continuum leads to a highly temperature dependent cross section that increases in importance relative to the bands as wavelength decreases toward 175 nm (Hudson and Mahle, 1972). These underlying continua must be considered when computing the solar energy that penetrates to any given level of the mesosphere and stratosphere.

The molecular parameters used to characterize the Schumann-Runge band cross section are (1) an oscillator strength for each vibrational transition and (2) a rotational line width in wavenumber units reflecting predissociation broadening for each band. Intercomparisons of the available laboratory data by Nicolet and Peetermans (1980), Nicolet (1983), and Frederick *et al.* (1983) show that significant discrepancies still exist. Of the measurements made over the last decade only those of Yoshino *et al.* (1983) have sufficient spectral resolution to yield the absolute cross section directly for the (1,0) - (12,0) bands. The cross sections of Yoshino *et al.* (1983) are recommended here as the preferred data set for future use in stratospheric modeling. However, these data, obtained at a temperature of 300 K, are not currently in a form that is directly applicable to atmospheric studies, although the necessary work is proceeding. The extraction of predissociation line widths from high resolution photoabsorption data for the (13,0) - (16,0) bands has been accomplished (Smith *et al.*, 1984) and the determination of line widths for the (1,0) - (12,0) bands is in progress (D. E. Freeman, personal communication, 1985).

Given band oscillator strengths and rotational line widths, it is necessary to compute the detailed cross section using the wavenumber and strength of each spectral line (Frederick and Hudson, 1979, 1980a). The total line width consists of contributions from predissociation and Doppler broadening while the line shape is described by a Voigt profile. Although Doppler broadening leads to a temperature dependent cross section, the major source of temperature sensitivity arises from absorption by $O_2(X^3\Sigma_g^-)$ in the excited $v=1$ and 2 levels. Band oscillator strengths for these transitions are typically an order of magnitude larger than for absorption by $v=0$ (Blake, 1979) leading to a temperature dependence in the total cross section that reflects a changing thermal population of the ground electronic state. In atmospheric applications this temperature dependence should be accounted for.

The atmospheric transmission of solar radiation in the i-th spectral interval for $i=1,2,\ldots,17$ as defined in Table 7-4 is:

$$T(i,N) = T_{SR}(i,N)\, T_{HZ}(i,N)\, T_{O_3}(i,N) \tag{7.9}$$

where $T_{HZ}(i,N)$ is the transmission as controlled by the Herzberg continuum of O_2, $T_{O_3}(i,N)$ accounts for the effect of absorption by ozone, and $T_{SR}(i,N)$ refers to the combined effects of the Schumann-Runge bands and the underlying Schumann-Runge continuum. Here N is the slant path O_2 column abundance measured along the path of the incoming solar beam. Because the O_2 Herzberg continuum σ_{HX} and ozone σ_{O_3} cross sections vary smoothly with wavelength one can use the mean values of Table 7-4 directly in the expressions

$$T_{HZ}(i,N) = \exp[-\sigma_{HZ}(i)N] \tag{7.10}$$

and

$$T_{O_3}(i,N) = \exp[-\sigma_{O_3}(i)\ N_{O_3}(N)] \tag{7.11}$$

where $N_{O_3}(N)$ is the slant path O_3 column at the location where N gives the slant column O_2. However, the rapid variation in the Schumann-Runge band cross section over small wavelength intervals makes it impractical, if not impossible, to include all spectral detail in photochemical calculations. For this reason simple parameterizations giving the transmission in a spectral interval or an effective cross section as a function of slant path molecular oxygen column content, N, are useful. An alternate approach is to present molecular oxygen dissociation rates and transmission values in tabular form. The transmission through the i-th spectral interval extending from wavenumber $\upsilon(i)$ to $\upsilon(i) + \Delta\upsilon(i)$ in the Schumann-Runge region is:

$$T_{SR}(i,N) = \frac{1}{\Delta\upsilon(i)} \int_{\upsilon(i)}^{\upsilon(i)+\Delta\upsilon(i)} d\upsilon \exp\left[- \int_{O}^{N} dN\ \sigma_{SR}(\upsilon,N)\right] \tag{7.12}$$

The cross section σ_{SR} depends on N because of temperature variations along the slant path of the incoming solar beam. As used here, the cross section, σ_{SR}, includes both the Schumann-Runge bands and Schumann-Runge continuum, but not the Herzberg continuum. Values of $T_{SR}(i,N)$ for the spectral range 57000–48500 cm^{-1} (λ = 175.439 – 206.186 nm) split into 17 intervals (i=1,2,..., 17) appear in Table 7-7. These calculations utilize the cross sections of Frederick and Hudson (1979, 1980a,b) applied to an overhead Sun and the temperature profile of the *U.S. Standard Atmosphere, 1976*. The temperature dependent Schumann-Runge continuum cross sections are from Hudson and Mahle (1972). The results of Table 7-7 can be applied to any solar zenith angle with acceptable accuracy by taking the tabulated O_2 column abundances to be measured along the slant path of incoming sunlight. In addition, the transmission values in Table 7-7 include an estimate of the effects of the (1,0) Schumann-Runge band covering intervals i=14 and 15. Absorption by this band was neglected by Frederick and Hudson (1979a, 1980a,b) since there was uncertainty as to whether predissociation occurs here, but it clearly appears in the high resolution stratospheric balloon spectra of Anderson and Hall (1983). Parameterizations incorporating varying levels of complexity have been presented by Blake (1979), Nicolet and Peetermans (1980), and Allen and Frederick (1982). Simon and Brasseur (1983) have reviewed the various approaches taken in this type of work. It would be of value to derive a new set of transmission functions and dissociation rates based on the cross sections of Yoshino *et al.* (1983) since these data are preferable to previous laboratory results because of their high spectral resolution. Such work has not yet been performed. Until this is done, the parameterizations of Nicolet and Peetermans (1980) or Allen and Frederick (1982), corrected to include currently accepted values of the Herzberg continuum cross section, are acceptable for atmospheric modeling.

7.1.6.3 Absorption by the Herzberg Continuum

Absorption by molecular oxygen in the Herzberg continuum, $A^3\Sigma_u^+ \leftarrow X^3\Sigma_g^-$, followed by dissociation is the dominant source of odd oxygen in the Earth's atmosphere at altitudes below approximately 60 km. The relevant wavelengths in the solar spectrum lie shortward of 242.4 nm. Despite the importance of this absorption in the formation of the ozone layer, the transition is strictly forbidden by electric dipole selection rules and the cross section is less than 1×10^{-23} cm^2 at all wavelengths.

Table 7-7. Transmission in the Schumann-Runge System (SR Bands Plus SR Continuum) Versus Slant Path O_2 Column

O_2Column N(cm^{-2})*	Transmission In 500 cm^{-1} Intervals**					
	(1) 57000-56500	(2) 56500-56000	(3) 56000-55500	(4) 55500-55000	(5) 55000-54500	(6) 54500-54000
3.922E+16	9.919E−01	9.947E−01	9.974E−01	9.979E−01	9.982E−01	9.994E−01
7.262E+16	9.851E−01	9.903E−01	9.952E−01	9.962E−01	9.967E−01	9.989E−01
1.555E+17	9.690E−01	9.807E−01	9.904E−01	9.920E−01	9.934E−01	9.977E−01
3.901E+17	9.274E−01	9.589E−01	9.784E−01	9.808E−01	9.849E−01	9.947E−01
1.060E+18	8.324E−01	9.183E−01	9.509E−01	9.533E−01	9.654E−01	9.868E−01
2.905E+18	6.666E−01	8.571E−01	9.003E−01	8.993E−01	9.291E−01	9.675E−01
7.718E+18	4.512E−01	7.698E−01	8.288E−01	8.166E−01	8.754E−01	9.294E−01
1.960E+19	2.416E−01	6.504E−01	7.398E−01	7.118E−01	8.045E−01	8.715E−01
4.716E+19	9.681E−02	5.013E−01	6.334E−01	5.910E−01	7.149E−01	7.989E−01
1.078E+20	2.584E−02	3.364E−01	5.087E−01	4.566E−01	6.060E−01	7.100E−01
2.358E+20	3.290E−03	1.823E−01	3.657E−01	3.160E−01	4.793E−01	6.014E−01
4.939E+20	8.669E−05	7.037E−02	2.140E−01	1.187E−01	3.422E−01	4.744E−01
9.919E+20	6.006E−08	1.479E−02	8.532E−02	7.962E−02	2.118E−01	3.365E−01
1.919E+21	0.000E−00	9.174E−04	1.636E−02	2.227E−02	1.050E−01	2.042E−01
3.607E+21	0.000E−00	4.659E−06	8.035E−04	2.992E−03	3.585E−02	1.003E−01
6.756E+21	0.000E−00	3.945E−10	5.405E−06	1.454E−04	7.271E−03	3.853E−02
1.299E+22	0.000E−00	0.000E−00	2.674E−09	1.750E−06	7.493E−04	1.085E−02
2.595E+22	0.000E−00	0.000E−00	0.000E−00	1.250E−09	2.147E−05	1.557E−03
5.382E+22	0.000E−00	0.000E−00	0.000E−00	0.000E−00	3.0380E−08	4.294E−05
1.145E+23	0.000E−00	0.000E−00	0.000E−00	0.000E−00	0.000E−00	3.130E−08
2.480E+23	0.000E−00	0.000E−00	0.000E−00	0.000E−00	0.000E−00	0.000E−00

Table 7-7. Transmission in the Schumann-Runge System (SR Bands Plus SR Continuum) Versus Slant Path O_2 Column (Continued)

O_2Column N(cm^{-2})*	Transmission In 500 cm^{-1} Intervals**					
	(7) 54000-53500	(8) 53500-53000	(9) 53000-52500	(10) 52500-52000	(11) 52000-51500	(12) 51500-51000
3.922E+16	9.997E−01	9.998E−01	9.999E−01	9.999E−01	9.999E−01	9.999E−01
7.262E+16	9.994E−01	9.997E−01	9.998E−01	9.999E−01	9.999E−01	9.999E−01
1.555E+17	9.989E−01	9.994E−01	9.997E−01	9.999E−01	9.999E−01	9.999E−01
3.901E+17	9.974E−01	9.987E−01	9.994E−01	9.997E−01	9.998E−01	9.999E−01
1.060E+18	9.933E−01	9.968E−01	9.986E−01	9.994E−01	9.994E−01	9.998E−01
2.905E+18	9.829E−01	9.918E−01	9.964E−01	9.984E−01	9.984E−01	9.996E−01
7.718E+18	9.598E−01	9.804E−01	9.910E−01	9.962E−01	9.959E−01	9.989E−01
1.960E+19	9.178E−01	9.588E−01	9.788E−01	9.908E−01	9.898E−01	9.974E−01
4.716E+19	8.567E−01	9.245E−01	9.560E−01	9.795E−01	9.763E−01	9.938E−01
1.078E+20	7.785E−01	8.745E−01	9.207E−01	9.581E−01	9.496E−01	9.862E−01
2.358E+20	6.828E−01	8.058E−01	8.741E−01	9.254E−01	9.035E−01	9.713E−01
4.939E+20	5.668E−01	7.158E−01	8.152E−01	8.759E−01	8.361E−01	9.452E−01
9.919E+20	4.302E−01	6.020E−01	7.404E−01	8.083E−01	7.516E−01	9.047E−01
1.919E+21	2.802E−01	4.603E−01	6.449E−01	7.167E−01	6.530E−01	8.493E−01
3.607E+21	1.455E−01	3.380E−01	5.272E−01	6.002E−01	5.427E−01	7.781E−02
6.756E+21	6.039E−02	2.227E−01	4.011E−01	4.720E−01	4.303E−01	6.917E−01
1.299E+22	2.027E−02	1.315E−01	2.827E−01	3.478E−01	3.273E−01	5.932E−01
2.595E+22	4.384E−03	6.138E−02	1.761E−01	2.296E−01	2.360E−01	4.831E−01
5.382E+22	2.953E−04	1.664E−02	8.453E−02	1.210E−01	1.532E−01	3.604E−01
1.145E+23	1.365E−06	1.443E−03	2.309E−02	4.147E−01	8.007E−02	2.306E−01
2.480E+23	0.000E−00	1.279E−05	1.948E−03	6.263E−03	2.716E−02	1.119E−01

Table 7-7. Transmission in the Schumann-Runge System (SR Bands Plus SR Continuum) Versus Slant Path O_2 Column (Continued)

O_2Column	Transmission In 500 cm^{-1} Intervals**				
$N(cm^{-2})$*	(13) 51000-50500	(14) 50500-50000	(15) 50000-49500	(16) 49500-49000	(17) 49000-48500
3.922E+16	9.999E−01	9.999E−01	9.998E−01	9.998E−01	9.999E−01
7.262E+16	9.999E−01	9.999E−01	9.998E−01	9.998E−01	9.999E−01
1.555E+17	9.999E−01	9.999E−01	9.998E−01	9.998E−01	9.999E−01
3.901E+17	9.999E−01	9.999E−01	9.998E−01	9.998E−01	9.999E−01
1.060E+18	9.999E−01	9.999E−01	9.998E−01	9.998E−01	9.999E−01
2.905E+18	9.998E−01	9.999E−01	9.998E−01	9.998E−01	9.999E−01
7.718E+18	9.997E−01	9.999E−01	9.998E−01	9.998E−01	9.999E−01
1.960E+19	9.993E−01	9.998E−01	9.998E−01	9.998E−01	9.999E−01
4.716E+19	9.983E−01	9.998E−01	9.996E−01	9.997E−01	9.998E−01
1.078E+20	9.962E−01	9.996E−01	9.996E−01	9.997E−01	9.998E−01
2.358E+20	9.921E−01	9.990E−01	9.994E−01	9.997E−01	9.998E−01
4.939E+20	9.846E−01	9.979E−01	9.984E−01	9.996E−01	9.996E−01
9.919E+20	9.728E−01	9.954E−01	9.977E−01	9.993E−01	9.995E−01
1.919E+21	9.546E−01	9.901E−01	9.954E−01	9.987E−01	9.990E−01
3.607E+21	9.274E−01	9.789E−01	9.910E−01	9.974E−01	9.983E−01
6.756E+21	8.881E−01	9.618E−01	9.827E−01	9.949E−01	9.970E−01
1.299E+22	8.365E−01	9.362E−01	9.679E−01	9.908E−01	9.944E−01
2.595E+22	7.687E−01	8.974E−01	9.403E−01	9.830E−01	9.891E−01
5.382E+22	6.763E−01	8.326E−01	8.859E−01	9.673E−01	9.783E−01
1.145E+23	5.511E−01	7.220E−01	7.810E−01	9.348E−01	9.553E−01
2.480E+23	3.896E−01	5.441E−01	5.947E−01	8.693E−01	9.076E−01

*O_2 column is measured along the slant path of incoming solar radiation.

**The numbering of intervals 1 through 17 is the same as that used in Table 7-4.

The small magnitude of the absorption poses major experimental problems, and it now appears that laboratory data used in atmospheric modeling prior to 1982 significantly overestimated the true cross section. A primary complication concerns the dependence of measured cross sections on the molecular oxygen concentration present in the laboratory apparatus. This arises from a combination of pressure-induced absorption and formation of the O_4 dimer whose absorption cross section differs from that of O_2. Historically, large O_2 column abundances were required to accurately measure the weak Herzberg continuum absorption, and in the laboratory this implied large concentrations as well. Data collected under such conditions require extrapolation to low pressure limiting values for application to upper atmospheric calculations. Apparently this pressure dependent behavior was not adequately corrected for in the early measurements, and published values for the zero pressure limit were not appropriate to atmospheric conditions. As an example of this pressure dependence, the data of Johnston *et al.* (1984) show a linear relationship between the measured absorption cross section and O_2 concentration. At a wavelength of 225 nm the cross section at one atmosphere is more than a factor of two greater than the zero pressure extrapolated value. An additional problem that may have degraded early data concerns unwanted formation of ozone in the laboratory system. Between 200 and 230 nm the absorption cross section of ozone exceeds that of molecular oxygen by factors ranging from 4×10^4 to 2×10^6. Hence a very small ozone mixing ratio in the laboratory system, if not corrected for, would seriously contaminate the derived Herzberg cross section, particularly at wavelengths greater than 220 nm. Further discussion of these issues appears in Frederick *et al.* (1983a) together with an intercomparison of cross section values published prior to 1980.

Balloon-borne spectrometer measurements of the attenuated solar irradiance reaching the middle stratosphere reported by Frederick and Mentall (1982) indicated more ultraviolet light reaching these levels than predicted on the basis of Herzberg continuum cross section values generally accepted at the time (e.g., Hasson and Nicholls, 1971; Ditchburn and Young, 1962; Ogawa, 1971; Shardanand and Prasad Rao, 1977; Hudson and Reed, 1979). Interpretation of the in situ measurements in terms of O_2 absorption cross sections by Herman and Mentall (1982a) implied values significantly less than the laboratory results. More recent balloon measurements by Anderson and Hall (1983) support these small cross sections, although the data of Pirre *et al.* (1984) suggest somewhat larger values. In addition, new laboratory work has been reported by Cheung *et al.* (1984a) and Johnston *et al.* (1984), taking care to derive the low pressure limiting cross sections properly. These support small values as inferred from the attenuated solar radiation measurements. However, a comparison of the results of Cheung *et al.* (1984a) and Johnston *et al.* (1984) in the wavelength region of near overlap shows a significant disagreement. In the wavelength range 204-205 nm Cheung *et al.* (1984a) report a cross section of $(5.5\pm1.0)\times10^{-24}$cm^2 while at 205 nm the Johnston *et al.* (1984) value is $(7.7\pm0.3)\times10^{-24}$cm^2. Both data sets are allegedly free of contamination from the long wavelength end of the Schumann-Runge bands. In yet unpublished work with longer path lengths and lower pressure A.S.C. Cheung and colleagues have examined in detail the extrapolation to the low pressure limit and obtain, at 205 nm, a cross section of $(7.2\pm0.2)\times10^{-24}$cm^2. These cross sections include a calculated Rayleigh scattering contribution (Bates, 1984) of 0.35×10^{-24}cm^2 at 205 nm.

The Herzberg continuum cross sections recommended in Table 7-4 are based on the laboratory results of Johnston *et al.* (1984) combined with a theoretical continuum shape to extrapolate in wavelength beyond the limits of the measurements, being 205 and 225 nm. The equation used for extrapolation is:

$$\sigma_{HZ}(\lambda) = \sigma_o \left(\frac{\lambda_o}{\lambda}\right) \exp\{-\alpha[\ell n(\lambda_o/\lambda)]^2\} \qquad (7.13)$$

where σ_{HZ} is the desired Herzberg continuum cross section at wavelength λ in nm. In the spectral range 205-225 nm Equation 7.13 was used to interpolate between the grid points of Johnston *et al.* (1984) using

σ_0 and α values obtained by fitting the measured cross sections at adjacent wavelengths. It is noted that the Herzberg continuum cross sections of Johnston *et al.* (1984) include contributions from Rayleigh scattering.

7.1.7 Absorption by Ozone

7.1.7.1 General Characteristics of Ozone Absorption

Absorption of incoming solar radiation by ozone occurs in the strong Hartley region at wavelengths less than 308 nm while the weaker, temperature dependent Huggins bands extend to longer wavelengths terminating near 360 nm. An additional absorption region, the Chappuis bands, lie in the visible from approximately 410 nm out through wavelengths exceeding 850 nm. Absorption in the Hartley region peaks close to 255 nm with a cross section near 1×10^{-17} cm^2 and is accompanied by the process $O_3 + h\upsilon \rightarrow O_2(a^1\Delta_g) + O(^1D)$ plus a small yield of $O(^3P)$. Absorption in the Huggins and Chappuis bands produces only ground state oxygen atoms. Simons *et al.* (1973) analyzed high resolution ozone spectra showing that the Hartley region is dominated by a continuum with weak band structure superimposed. The electronic transition is $^1B_2 \leftarrow X^1A_1$. The Huggins bands involve the same upper and lower states where absorption here populates $^1B_2$ below the dissociation limit followed by predissociation.

7.1.7.2 The Hartley Region

Absorption in the Hartley region is by far the dominant mechanism for dissociating ozone in the stratosphere and mesosphere. Over the past 35 years there have been several measurements of the cross section as reviewed by Hudson (1971) up through 1970. Hearn (1961) reported absolute measurements of the Hartley region cross section at the wavelengths of several mercury lines, 253.7, 289.4, 296.7, and 302.1 nm, and these results have served as the basis for normalizing relative measurements that cover the entire spectrum. Absolute values of the Hartley region cross section are generally considered known to an accuracy of $\pm 2.5\%$ at room temperature.

The recommended cross section values in Table 7-4 are based on the following original data sources and previous tabulations. For spectral intervals i=1 to 14 (λ = 175.439 - 200.000 nm) the values are based on the data of Watanabe *et al.* (1953) as tabulated by Ackerman (1971). There appears to have been no new measurements reported in this wavelength region since 1953. Recommended cross sections for intervals i=15 to 33 (λ = 200.000 - 246.914 nm), also taken from Ackerman (1971), are based on the results of Inn and Tanaka (1953) which are supported by the later measurements of DeMore and Raper (1964) and Griggs (1968). New measurements for spectral intervals i=34 to 57 (λ = 246.914 - 347.5 nm) encompassing essentially all of the remaining Hartley region have been made by A.M. Bass of the National Bureau of Standards and R.J. Paur of the Environmental Protection Agency (Bass and Paur, 1984; Paur and Bass, 1985). These results, which are not yet published in full, include the temperature dependence of the cross section and use the 253.7 nm measurement of Hearn (1961) to establish an absolute scale. The cross section at 253.7 nm is assumed to be independent of temperature. Table 7-4 lists the Bass and Paur cross sections at temperatures of 203 and 273 K, a range that encompasses that encountered in the stratosphere. The temperature dependence seems to arise from absorption by excited modes of $O_3(X^1A_1)$ in the thermal population (Simons *et al.*, 1973). Near the long wavelength limit of the Hartley region (i=49) the ratio of cross sections for 273 K and 203 K is 1.11. While this variation is not large compared to many uncertainties in photochemical modeling, the temperature dependence of the Hartley region should likely be included in future atmospheric calculations at wavelengths greater than 295 nm. At wavelengths

greater than 300 nm where the quantum yield of $O(^1D)$ in ozone photodissociation is temperature dependent, simultaneous measurements of the absolute cross section and of the production of $O(^1D)$ are still needed as functions of temperature.

7.1.7.3 The Huggins Bands

At wavelengths greater than 310 nm the vibrational structure of the Huggins bands becomes pronounced and the cross section displays a significant temperature dependence as illustrated at low spectral resolution by Table 7-4. When the spectral structure associated with bending and symmetric stretching sequences is resolved as in the data of Simons *et al.* (1973), the cross section at locations in between the sharp peaks shows a large temperature dependence with much smaller changes in the immediate vicinity of cross section maxima. These variations reflect a changing thermal population of vibrational levels in the ground electronic state.

Early cross section determinations in the Huggins bands by Inn and Tanaka (1953) and Griggs (1968) show generally good agreement, although the fine structure in the spectrum makes the measured result dependent on details of the instrument bandpass. Results obtained at high spectral resolution (0.003 nm) by Freeman *et al.* (1984) reveal structure in the Huggins bands on wavelength scales of 0.01 to 0.02 nm. Freeman *et al.* (1984) also intercompared various high resolution data sets over the wavelength range 323-327 nm and found differences between absolute values that can be 20 percent or more. This is indicative of a temperature dependence and, to a lesser extent, discrepancies in reported absolute values. Because of fine structure in the ozone absorption cross section and the temperature dependence, the level of agreement between different data sets in the Huggins bands is not yet satisfactory.

Since for use in photochemical modeling cross sections averaged over broad spectral intervals are required, the values in Table 7-4 are adopted. However, this totally obscures the fine structure in the true cross section. For application to atmospheric ozone measurements it is essential to consider details of the Huggins bands cross section that lie within the instrument bandpass. Table 7-4 lists the recommended Huggins band cross section values for temperatures of 203 and 273 K beginning with spectral interval i=50. The reported values are derived from the high resolution results of Bass and Paur (1984). Tabulated cross sections for i=58 to 60 are based on Inn and Tanaka (1953) as tabulated by Ackerman (1971). Based on the analysis of Simons *et al.* (1973) the cross section in these last three spectral intervals arises entirely from absorption by thermally excited $O_3(X^1A_1)$ and rapidly becomes negligible below typical room temperatures. Over the wavelength range 362.5 to 407.5 nm (i=61 to 69) absorption by ozone is weak and is insignificant at stratospheric and mesospheric temperatures. A new set of accurate, absolute cross section measurements covering the entire Huggins bands, including temperature dependence, would be of value for atmospheric applications.

7.1.7.4 The Chappuis Bands

Ozone absorbs weakly in the visible region of the spectrum via the Chappuis bands that extend longward of 407.5 nm and peak near 600 nm with a cross section close to 5×10^{-21} cm^2. The original data source for the cross sections of Table 7-4, beginning with interval i=70, is Vigroux (1953) whose results have been confirmed by Griggs (1968). The values of Table 7-4 for i=70 to 117 are as given by Ackerman (1971) and for i=118 to 158 are from Nicolet (1981). The accuracy of the available data, as indicated by the agreement between Vigroux (1953) and Griggs (1968), is sufficient for applications to atmospheric modeling.

For many atmospheric applications it is not necessary to include the spectral detail of Table 7-4 at Chappuis band wavelengths. Therefore, Table 7-8 presents the Rayleigh scattering cross sections, and ozone absorption cross sections averaged over 50 nm intervals extending from 375 to 875 nm. The values are as given by Nicolet *et al.* (1982).

Table 7-8. Reference Rayleigh Scattering and Ozone Absorption Cross Sections Averaged Over 50 nm Intervals

Central Wavelength (nm)	Rayleigh Scattering $\sigma_{RS}(cm^2)$	Ozone Absorption $\sigma(O_3)$ (cm^2)
400±25	1.67E-26	—
450	1.03E-26	2.34E-22
500	6.66E-27	1.25E-21
550	4.51E-27	3.39E-21
600	3.17E-27	4.46E-21
650	2.29E-27	2.47E-21
700	1.70E-27	9.75E-22
750	1.28E-27	3.85E-22
800	9.88E-28	2.05E-22
850	7.74E-28	—

7.1.8 Solar Heating Rates

The calculation of accurate atmospheric heating rates by absorption of solar radiation is, in principle, straightforward provided the proper input data are available. For an aerosol-free atmosphere the required information consists of the incident solar spectral irradiance, the absorption cross sections of O_3 and O_2, the Rayleigh scattering cross section, and the vertical distribution of ozone at all locations. The dominant processes for heating the stratosphere and mesosphere are dissociation of O_3 and O_2 where calculations assume that all excess energy above that needed to break the molecular bond is thermalized. Absorption of solar radiation by NO_2 also makes a small contribution to stratospheric heating, being up to 0.1 K per day. Complications inherent in the heating rate evaluation concern the need to include multiple scattering and reflection from the lower boundary of the atmosphere. The parameterization of Lacis and Hansen (1974), which includes all of the above processes, has wide acceptance here, although the availability of improved values of the solar irradiance, the relevant cross sections, and of vertical profiles of ozone in the stratosphere and mesosphere would make a new evaluation of value. Such work has recently been performed by Kiehl and Solomon (1986) using LIMS measurements.

When volcanic aerosols are present in the stratosphere the problem of evaluating the heating rate becomes much more complex. Pollack and Ackerman (1983) have shown that a lower stratospheric aerosol layer like that from El Chichon could lead to an extra heating of several tenths of a degree per day.

Figure 7-7 from London (1980) illustrates the latitudinal and seasonal pattern in the heating rate by O_3 and O_2. Large values exist in the high latitude summer with the maximum absorption per unit mass occurring near 50 km where the heating is 18 K per day. This peak value determines the location of the stratopause (London, 1980). The increase in heating rate at altitudes above 70 km arises from absorption by molecular oxygen. Finally, the heating rate in the mid-to-high latitude winter is generally less than 2 K per day. Although use of more recent data would alter the values in Figure 7-7, the overall patterns with latitude and season are well-established. However, the relevant quantity for dynamical modeling is the difference between the heating and cooling rates, the latter arising from terrestrial emission. Small errors in either calculation could have a significant impact on the accuracy of the final net heating rate. Therefore, as improved data become available they should be used to generate updated heating rates in a timely manner. This is especially true of the global distribution of ozone for which an ever increasing data base exists.

7.2 TERRESTRIAL RADIATION

7.2.1 Overview and Major Issues

In the absence of motions the thermal structure of the stratosphere and mesosphere would be determined solely by a balance between heating arising from absorption of solar radiation and cooling by infrared emission. Because of the circulation, the actual thermal structure departs greatly from this state of radiative equilibrium and is determined by all three components. Accurate treatments of both solar and infrared radiation are therefore critical components of general circulation models. Furthermore, infrared emission exerts a significant influence over the evolution of atmospheric eddies via radiative damping. This section assesses the present knowledge of terrestrial longwave radiation and identifies the major issues requiring additional study.

Several recent studies illustrate the effect of the interplay between net heating and circulation on trace gas distributions. Transport by the large-scale circulation can be decomposed into two components: meridional mixing on isentropic surfaces and zonal mean cross-isentropic transport due to net radiative heating of air parcels, the *mean diabatic circulation* (Mahlman *et al.*, 1981, Tung, 1982). Harwood and Pyle (1980), using a zonally symmetric model, calculated the change in total ozone caused by changing the radiation and the corresponding diabatic circulation in the lower stratosphere. The change in radiation was accomplished by incorporating Rodgers' (1967) heating rates in the lower stratosphere where they had previously assumed no heating. The magnitude of this change was only a few tenths K day^{-1}. The corresponding change in ozone is substantial, especially near 30N and 30S in July–September where changes of 20% in total ozone column are found. This change is significant compared with current model estimates of decreased ozone column due to increases in CFC's of roughly 5%.

Haigh (1984, also see Haigh and Pyle, 1982) has examined the differences in ozone distribution and total ozone in the Harwood-Pyle model between a case with fixed heating rate and a case with the heating rate calculation fully coupled to the modeled variations of temperature and ozone. In the lower stratosphere between 150 and 30 mb, total column ozone differences of 10-20% were produced even though heating rate differences were only a few tenths of a degree Kelvin per day. These differences were attributed to differences in the strength of the zonally symmetric meridional circulation.

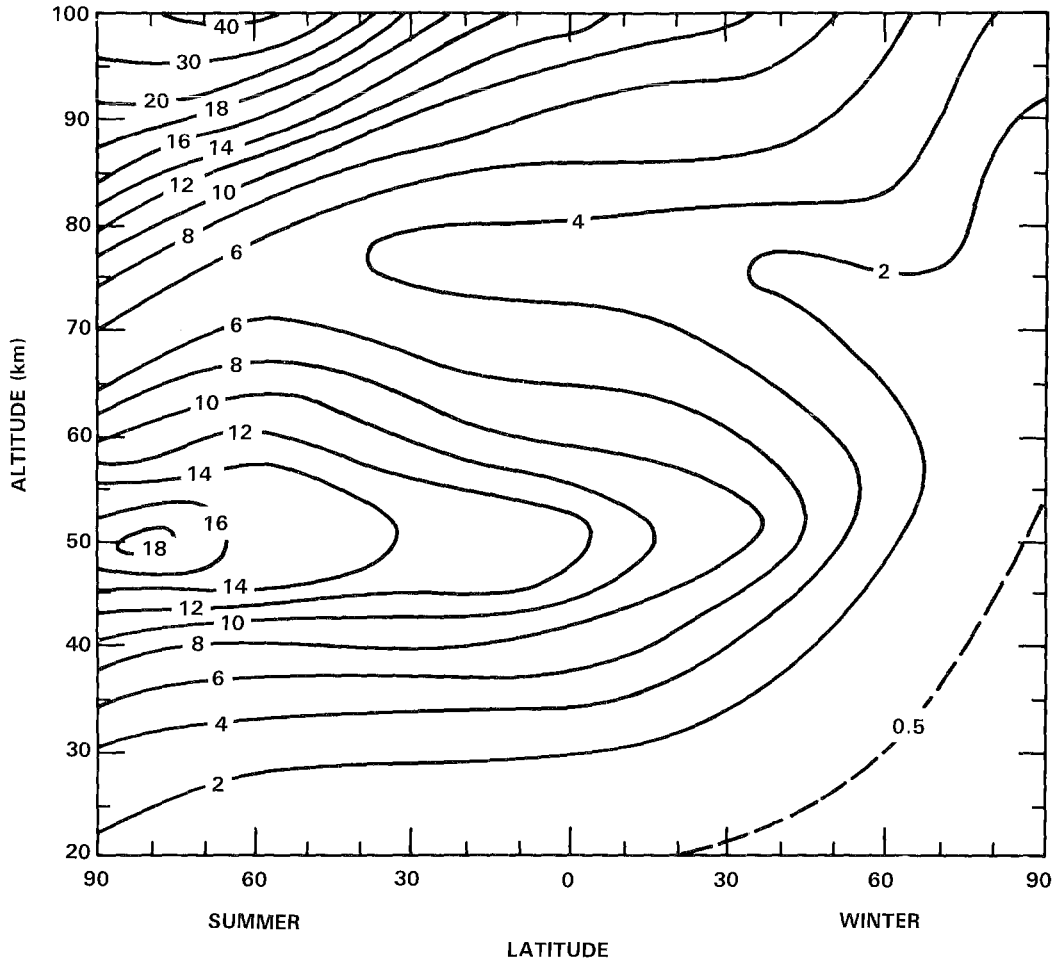

Figure 7-7. Heating rate arising from absorption of solar radiation by ozone and molecular oxygen. Values are in K per day from London (1980).

Simulations of the circulation of the middle atmosphere depend on a delicate interplay between the modeling of radiative forcing and forcing by eddies. The latter is often described quantitatively as the *Eliassen-Palm flux divergence* (EPFD). Experiments by Ramanathan *et al.* (1983) using the NCAR Community Climate Model have demonstrated model sensitivites to relatively modest changes in the treatment of radiative forcing in the lower stratosphere. They degraded the model radiation scheme by altering the upper boundary condition for solar absorption, eliminating the temperature dependence of the CO_2 hot bands and changing the temperature dependence of H_2O emissivity. The largest changes occurred in the polar night region of the stratosphere where temperatures decreased by as much as 25K.

The objective of longwave radiation calculations is to predict the heating or cooling at a given location in the atmosphere associated with absorption and emission of terrestrial radiation in the infrared. Numerical simulations of longwave heating and cooling must treat details of radiation transfer in the infrared bands of CO_2, O_3, H_2O, and other trace gases. This requires either lengthy line-by-line calculations or accurate band models to treat the transmission of thermal radiation through a broad spectral region containing numerous individual lines. The major issues in these investigations involve (1) the accuracy of line-by-line computations,

(2) the accuracy and completeness of spectroscopic data required in the evaluations, and (3) the availability and accuracy of band models. These topics together with an assessment of the role of terrestrial radiation in atmospheric dynamical modeling receive attention in the following sections.

7.2.2 Line-by-Line Calculations, Band Transmittances, and Spectroscopic Data

The transmittance of terrestrial radiation through a wavenumber interval $\Delta\upsilon$ is defined as:

$$A = \int_{\Delta\upsilon} [1-\exp(-\int k_{\upsilon}(s)\varrho(s)ds)]d\upsilon \tag{7.14}$$

where $\varrho(s)$ is absorbing gas density, k_{υ} is the mass absorption coefficient and integrations are over path-length elements ds and bandwidth $\Delta\upsilon$. The complexity in applying Equation 7.14 to atmospheric radiation transfer derives from the fact that k_{υ} varies rapidly over the interval $\Delta\upsilon$ displaying a line structure characteristic of the molecular band under consideration, for example, the 15 micron band of CO_2 or the 9.6 micron band of ozone. The absorption coefficient is also a function of pressure and temperature and varies along the inhomogeneous paths that occur in the atmosphere.

Presently, there are three general techniques available for examining longwave radiation transfer in the atmosphere. First, calculations that accurately resolve the structure of each rotational line in the infrared spectrum can be carried out. These line-by-line methods can be very accurate, but they are computationally very expensive. For this reason, the line-by-line models are most often used as 'benchmarks' to gauge how well parameterized methods are able to capture the important radiative properties of the atmosphere. Secondly, calculations can be performed for narrow spectral intervals that do not resolve the structure of each rotational line. These narrow band models make certain assumptions regarding the distribution of line strengths and positions within each narrow spectral interval. The definition of 'narrow' interval has in the past been very subjective. Intervals ranging from 2 cm^{-1} to 200 cm^{-1} have been employed to model the absorption of a given gas. Recently, Kiehl and Ramanathan (1983) have shown that narrow band model results are quite sensitive to interval size. It was found that an interval size of a few cm^{-1} (5 cm^{-1} for the case of CO_2) led to good agreement between observed and calculated absorption. A more detailed discussion of the problems involved with the narrow band model appears in Chapter 15 of this report. Finally, the third method available for examining the radiative budget is the broadband model. Because of their dependence on a number of assumptions regarding the structure of the band and the treatment of temperature and pressure dependence, the exact formulations of these models tend to differ from one another. The advantage of these models is their great computational speed. Thus, they are well suited for large general circulation models. They have also been shown to be in good agreement with observed absorptances and higher resolution models (Kiehl and Ramanathan, 1983, Ramanathan and Downey, 1985; Fels and Schwarzkopf, 1981). For the stratosphere, there is good agreement between these models. Cooling rates generated by both narrow and broadband models are within 5–10% of one another throughout the stratosphere.

The objective of line-by-line calculations is to construct a detailed model of k_{υ} as a function of υ in Equation 7.14 including all temperature, pressure, and path length dependencies. The major scientific concerns involve the accuracy with which such models represent the actual transfer of radiation in the Earth's atmosphere. The parameters needed to construct k_{υ} are the position in wavenumbers of the center of each line in the band, the intensity of each line, the line widths, and the shapes of the line profiles. The positions of the lines can be computed from standard formulae tailored to each molecule, although reliable molecular constants must be based on accurate spectroscopic data. It is important to include the

variation of line widths with temperature, and this is not necessarily a simple square root dependence as is often assumed. It is also necessary to obtain line widths at typical atmospheric pressures to circumvent possible errors encountered in extrapolation from laboratory conditions.

Figure 7-8 from Chedin and Scott (1984) illustrates the fact that transmittances computed for the 15 micron CO_2 band using laboratory measurements of line half-width and assuming a Lorentzian shape can overestimate transmittance. At low pressures characteristic of the upper stratosphere, synthetic spectra based on Lorentz or Voigt line shapes are generally in good agreement with observed spectra. However, depending on the particular molecule, this agreement degrades toward higher pressure. This issue is particularly important for remote sensing of atmospheric composition. The situation is less delicate for energy balance calculations. Fels (1985) notes that the product of line strengths and line widths in transmission calculations is less uncertain than either quantity individually, and as a consequence, these uncertainties are not the limiting factor in heating rate calculations for the middle atmosphere.

A good indirect indication of the reliability with which the spectroscopic parameters of CO_2, O_3, and H_2O are known can be obtained by considering the problem of stratospheric remote sensing. In general, remote sensing places more stringent requirements on the accuracy of spectroscopic parameters than do heating rate calculations. Although there are some systematic discrepancies, some of which may be due in part to errors in spectroscopic data, agreement between limb sounding retrievals and correlative measurements of temperature, ozone, and water vapor are generally excellent (Gille *et al.*, 1984a; Remsberg *et al.*, 1984a; Russell *et al.*, 1984c), and this result lends strong credence to the accuracy of the spectroscopic parameters used in these retrievals.

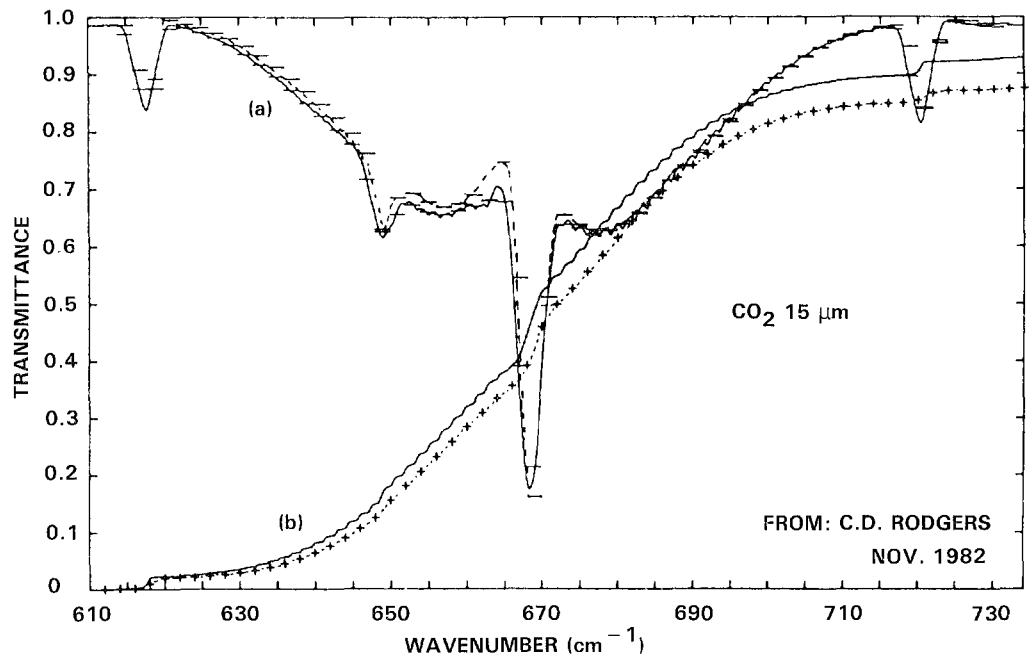

Figure 7-8. Laboratory and synthetic spectra of CO_2 in the 15 micron spectral region. (a) Solid curve: synthetic spectrum; dashes: observations. (b) Integrated absorption. Solid curve: synthetic; dashes: observations. (from Chedin and Scott, 1984; figure originally from C. D. Rodgers, private communication, 1982).

Drayson *et al.* (1984) have discussed the spectroscopic data used in these calculations. For CO_2, the AFGL tape (1975 version) was used and proved to be satisfactory. The principle uncertainties are in the precise strengths of the bands and in the shape of the pressure broadened lines in the far wings. These are known to be sub-Lorentzian (Fels and Schwarzkopf, 1981). Overall, the accuracy of the spectroscopic data base for the 15 μm CO_2 bands should be sufficient to allow transmission function calculations that are accurate to within at least 10%, and probably better than 5%, throughout the middle atmosphere.

The water vapor rotation band and 6.3 μm band parameters are also well known, and the parameters on the AFGL tape are probably as accurate as those for CO_2. The water vapor lines are super-Lorentzian in the far wings, but the effect of this on heating rate calculations is very small (Thomas and Nordstrum, 1982).

Spectroscopic parameters for O_3 are the least well known of the three gases. Drayson *et al.* used the data of Flaud *et al.* (1980) with a modification to band strength recommended by Secroun *et al.* (1981). The line strengths and positions in the isotopic bands of $O^{16}O^{16}O^{18}$ and $O^{16}O^{18}O^{16}$ are not very well known, and there is still some uncertainty about the temperature dependent line half-widths and line shapes. Nevertheless, the overall accuracy of transmission functions for this band should exceed 10% (Drayson *et al.*, 1984). Because the ozone contribution to the middle atmosphere cooling rate is generally less than 1/3 as large as that for CO_2, uncertainty in ozone spectroscopic parameters should make a relatively small contribution to heating rate errors.

For modeling of atmospheric energetics and dynamics the required quantity is the transmittance over an entire band. It would be of great value to measure these quantities directly in the laboratory using broadband instruments over the range of pressure and temperature characteristic of the atmosphere. At typical laboratory temperatures "hot bands" arising from absorption by thermally excited states are present and would alter the measured transmittance from that applicable to the stratosphere and mesosphere. Broadband measurements would provide an important constraint on line-by-line calculations. Once given line-by-line results that are accurate over a range of atmospheric conditions, it is then possible to develop reliable band models. Spectroscopic properties of such trace gases as CH_4, N_2O, HNO_3 and CFC11 and 12 are not as well known as those of CO_2, H_2O, and O_3. Although the contribution of these gases to the net cooling rate is now relatively small, their concentrations are expected to increase and laboratory measurements of broadband transmittance over the proper range of temperature and pressure would be of direct use in climate studies as well as remote sensing.

7.2.3 Radiative Damping

Under suitable conditions, the behavior of eddies can be strongly influenced by the damping effect of long wave radiative emission. This problem has been the subject of a number of studies in the last several years (Fels, 1982; Wehrbein and Leovy, 1982; Schoeberl, *et al.*, 1983; Fels, 1984; Apruzese and Strobel, 1984). After a period of some initial disagreement, when it seemed that there was a substantial spread in the theoretical relaxation rates calculated by different investigators, there now seems to be a satisfactory consensus on this subject. A major concern in this research has been an evaluation of the dependence of the damping rate on the vertical scale of the wave. A second issue, important for mesospheric calculations, has been the incorporation of effects due to the breakdown of local thermodynamic equilibrium.

The results of the above studies show that scale dependent radiative damping is of considerable importance in the dynamics of waves whose vertical wavelength is shorter than 30 km. At 50 km, for example, a disturbance of wavelength 12 km will decay about three times as rapidly as will one whose wavelength

is infinite (Fels, 1984). This and other cases are illustrated in Figure 7-9. These effects can be of considerable importance not only for the waves themselves, but also for related large scale phenomena whose behavior depends on wave damping, such as the quasi-biennial oscillation (Holton and Lindzen, 1972; Hamilton, 1981b), the zonal mean momentum budget of the mesosphere (Holton, 1982), and the semiannual oscillation (Hitchman and Leovy, 1986).

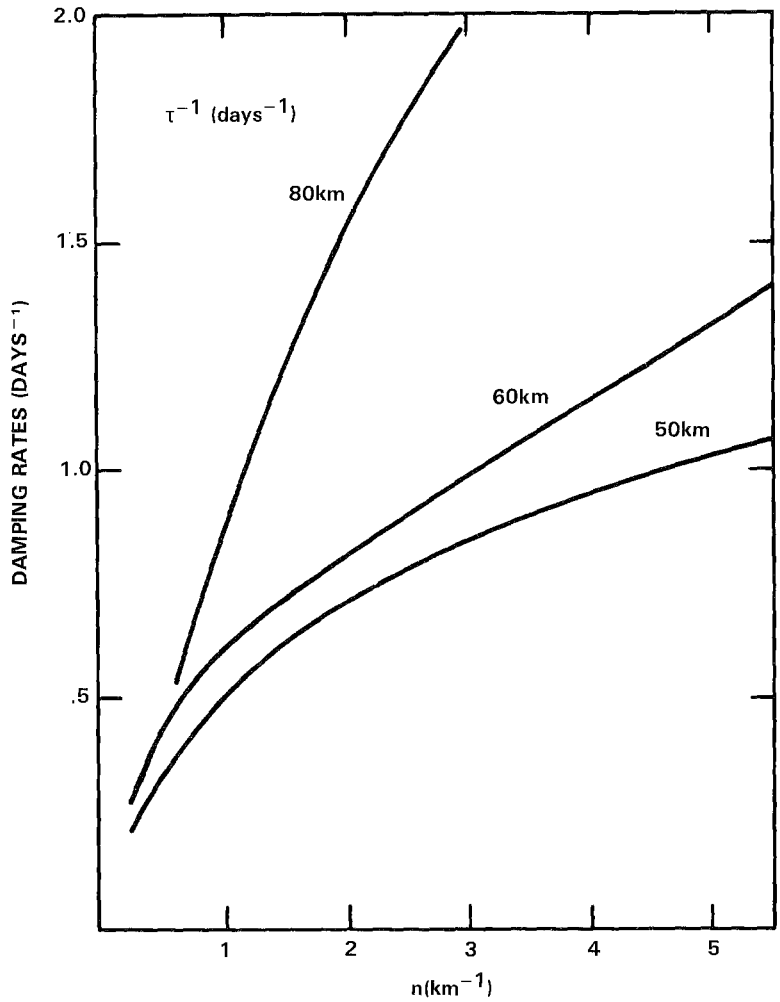

Figure 7-9. Middle atmosphere damping rates (ordinate, days^{-1}) versus vertical wavenumber n (km^{-1}). From the calculations of Fels (1982, 1984).

For internal gravity waves whose vertical scale is on the order of a kilometer or less, the decrease of damping time with decreasing wavelength is slow. To the extent that turbulent mixing behaves as a diffusive process, radiative decay should not play an important role in the damping of disturbances of very small vertical scale in the middle atmosphere. In contrast to internal gravity waves and most classes of equatorial waves, planetary waves have vertical scales large enough that radiative damping is dominated by radiation to space and is therefore essentially scale independent (vertical wavelengths ≥ 30 km). It is therefore likely to be less important for these waves. However, an interesting question arises in connection with the influence of radiative damping of the potential vorticity field (McIntyre and Palmer, 1984). As

inferred from global satellite radiance measurements, this field appears to show rather rapid nonconservative changes in the middle and upper stratosphere during disturbed wintertime conditions (major and minor warmings). Detailed calculations of the extent to which these changes are due to diabatic processes as opposed to turbulent motions at scales that are not resolved by the available data have not been published.

A final issue concerns the photochemical acceleration of radiative damping. Physically, a temperature perturbation which alters the local thermal emission also influences the ozone abundance via a change in the reaction rates that govern odd oxygen loss. The effect is to alter the local solar heating rate in a manner to accelerate the decay of the initial perturbation. Recently, Ghazi *et al.* (1985) have used simultaneous ozone and temperature measurements to study radiative damping in the stratosphere. Empirically they show that changes in upper stratospheric solar heating accelerate the damping rate in a manner that supports the more recent theoretical predictions of Hartmann (1978) and Strobel (1978) and previous atmospheric observations (Ghazi *et al.*, 1979).

7.2.4 Longwave Radiation in the Stratosphere

The calculation of long wave cooling is relatively straightforward near the stratopause, but becomes increasingly difficult as one descends into the lower stratosphere. In part, the difficulty arises from the contributions of species other than CO_2, O_3, and H_2O, particularly aerosols. It is also due to the relatively great contribution in the lower stratosphere of upwelling radiation from the troposphere. Below about 25 km the net radiative imbalance is determined by a small difference between several heating and cooling contributions each of which is individually very small.

Variable tropospheric cloudiness is an additional problem in net heating calculations. Between 20 and 25 km, two of the largest contributors are heating due to absorption of solar radiation in the visible and ultraviolet bands of ozone and exchange of long wave radiation by ozone in the 9.6 μm band which is also generally a heating effect below 25 km. The former can vary by up to 30% as a result of variations in the albedo of underlying surface and cloud, while the latter can vary by as much as 100% as a result of variations in the height, coverage, and emissivity of clouds. Each of these factors can contribute up to 0.5 K day^{-1} to heating in the 20–25 km layer (London, 1980a).

The spatial distribution of the total longwave cooling can be calculated with any of the methods mentioned in Section 7.2.2. The zonally averaged longwave cooling for the month of January is shown in Figure 7-10. A narrow band Malkmus model employing an interval size of 5 cm^{-1} and using the Voigt line profile of Fels (1979) was used for these cooling rate calculations (Kiehl and Solomon, 1986). The temperature and gas distributions are from the monthly and zonally averaged January LIMS data (Gille and Russell, 1984). The lower stratosphere is radiatively cooling everywhere except near the tropical tropopause region. The relative magnitude of the cooling/heating in the lower stratosphere is only a few tenths K per day. Note that the maximum latitudinal range of cooling near 26 km is larger than a factor of 2. The region of warming around the tropical tropopause is very sensitive to the mean thermal state. If the temperatures in this region were increased by 5 K this region would radiatively cool.

As pointed out above, this region is also affected by the presence of clouds. In the tropics cirrus clouds occur not only below the tropopause, but also at times just above the mean tropopause. The presence of cirrus in this region can greatly change the local radiative energy budget. The results of Stephens and Webster (1979) for a layer of cirrus imply large longwave cooling at the cloud top and moderate solar heating in this region. The net radiative effect for their high cloud case is a cloud top cooling of a few

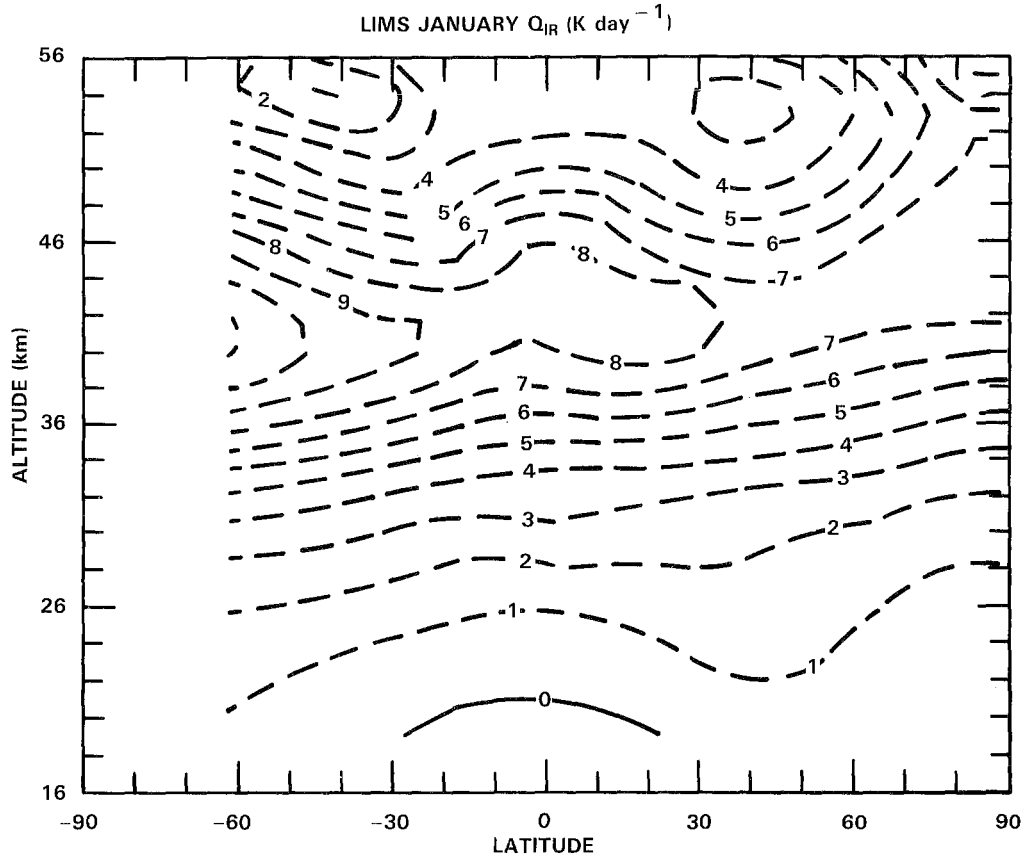

Figure 7-10. Zonally averaged longwave cooling rates for the mean January LIMS data in K day^{-1} (Kiehl and Solomon, 1985).

K per day. Since the solar heating is present only during the daytime, large diurnal variations in this cooling will exist. The cooling due to cirrus is strongly dependent on the height of the cloud as well. The emissivity of these clouds is also an important radiative property. Cirrus are not black as is commonly assumed for cloud forms at lower levels. Another important property which affects the cloud top cooling is the cloud microphysics. Ramaswamy and Detwiler (1985) have calculated the cloud top cooling of a cirrus layer as a function of the crystal length. Their results indicate that this cooling is dependent on cloud microstructure. These studies show that an accurate knowledge of the cloud morphology and microphysics is necessary for a detailed determination of the radiative cooling in and above the cloud and into the lower stratosphere. Figure 7-11 shows the results of the calculations of Ramanathan *et al.* (1983) of the effects of cirrus on net radiative heating.

The presence of volcanic aerosols can also affect the radiative balance of this region. The computed change in net longwave radiative heating based on the radiation model of Ramaswamy and Kiehl (1985) due to background aerosols (McClatchey *et al.*, 1971) and El Chichon aerosols (Hoffman and Rosen, 1983) is shown in Figure 7-12. The change due to the background aerosol layer is very small (0.003 K per day), but the magnitude of change due to the El Chichon volcanic cloud is comparable in magnitude to the net longwave heating of the unperturbed stratosphere (0.4 K per day). The predicted effect of El Chichon volcanic aerosols on the heating rate due to absorption of solar radiation was also found to be significant

if the aerosols contained 10% or more ash by volume. Radiative-convective equilibrium calculations for the El Chichon cloud with 10% ash give a temperature increase of 3.5K at 24 km, (Pollack and Ackerman, 1983) in agreement with the observational estimate of Labitzke *et al.* (1983). These calculations also indicate that the El Chichon cloud had a non-negligible influence on the heat balance of the troposphere. Such large stratospheric changes could affect the quasi-biennial oscillation (Dunkerton, 1983b). Kiehl (1984) has also pointed out the importance of stratospheric aerosols in changing radiative damping rates in this region of the stratosphere. Thus, knowledge of the transient volcanic events is of great importance in understanding the radiative balance of the lower stratosphere.

Though less important than volcanic aerosols following major eruptions, polar stratospheric clouds can also influence the net radiative heating. These clouds occur frequently in the Southern Hemisphere winter polar vortex and occasionally in the Northern Hemisphere polar vortex in the 15-25 km layer

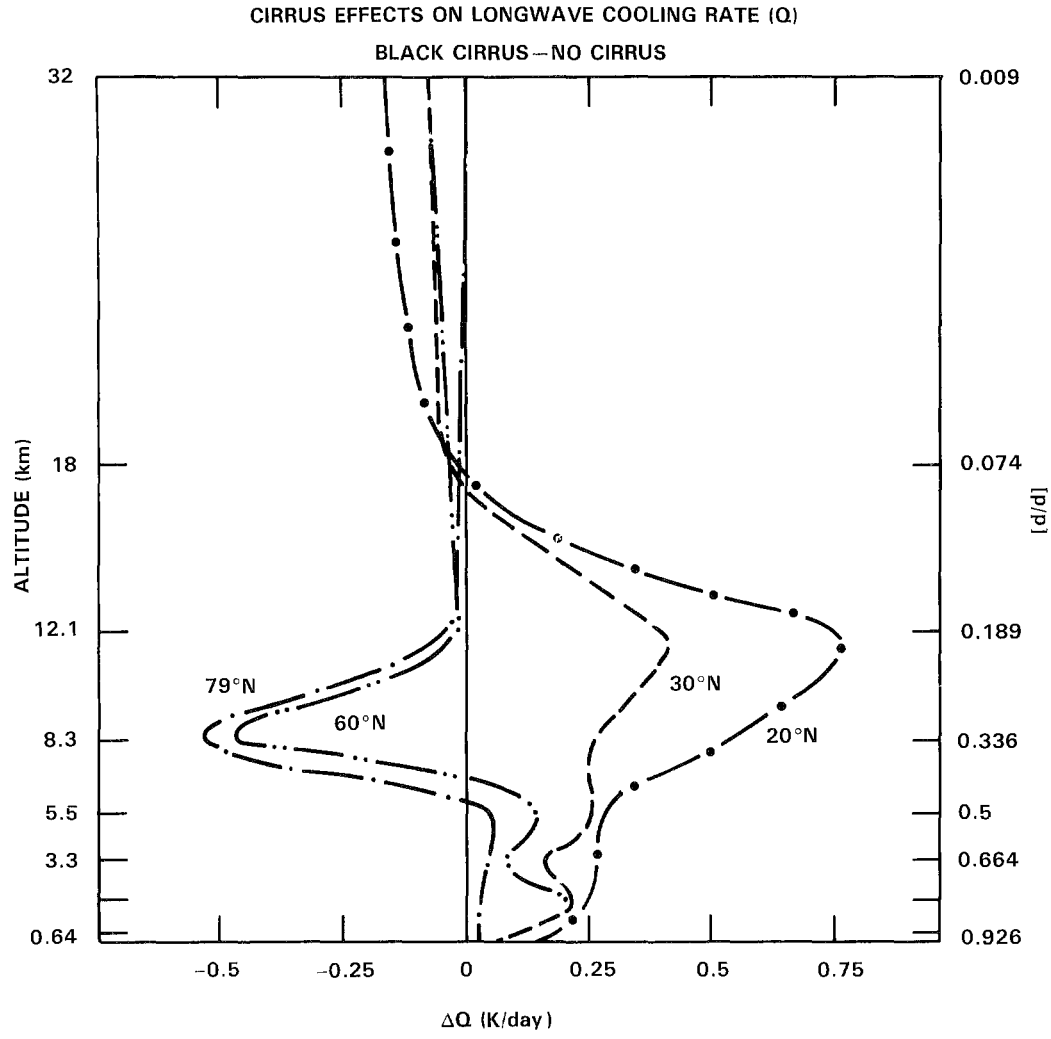

Figure 7-11. Change in net radiative heating due to the effect of prescribed black cirrus at various latitudes (Ramanathan *et al.*, 1983).

(McCormick *et al.*, 1982). Their effect on the radiation is ordinarily small, but they might occasionally make a significant contribution to the budget in the Antarctic (Pollack and McKay, 1985). More work to define the radiative properties of these clouds would be of value.

The role that other gases can play in determining the radiative and thermal structure of the lower stratosphere and tropopause region must also be considered. The change in the tropical longwave cooling due to the presence of CH_4, N_2O, CF_2Cl_2 and $CFCl_3$ is only a few hundredths of a degree per day, but due to the spectral position of the absorption bands of these gases, they tend to radiatively heat the tropopause region. Thus, an increase in the amount of any of these gases will lead to an increase in heating in this region. This effect could have important implications for the abundance of H_2O in the stratosphere.

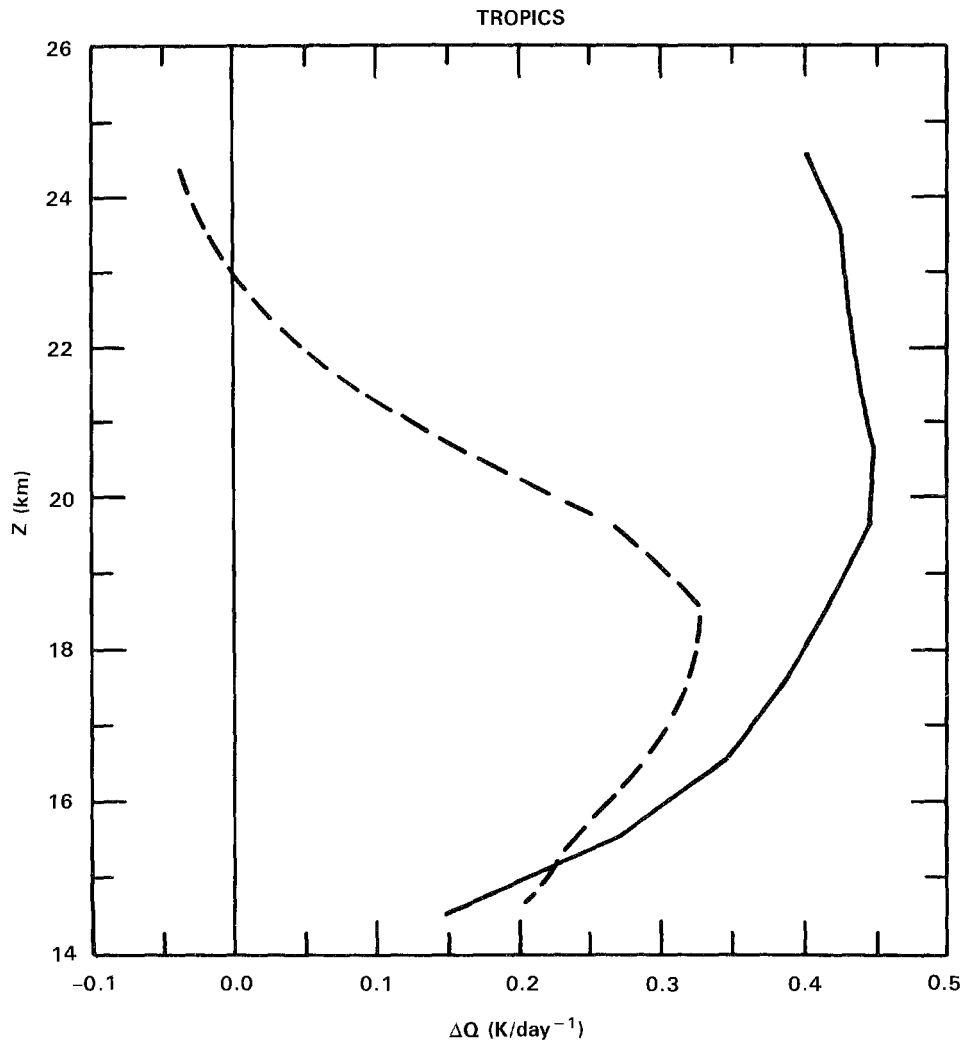

Figure 7-12. The change in net longwave heating rates due to the presence of background aerosols (dashed: for this case cooling has been multiplied by a factor of 100), and the El Chichon aerosol layer (solid).

The accuracy of radiative cooling calculations depends on the accuracy of the input data used to evaluate the radiative fluxes. As discussed in Section 7.2.2, the input data for these calculations are the line strength, width, and position. An estimate of how inaccuracies in these parameters can affect the radiative cooling can be obtained by varying any one of these parameters by a given amount, and then evaluating the cooling for the new 'adjusted' line parameters. The results of a calculation where the line strengths of CO_2 were increased by 10% are shown in Figure 7-13 using the model described by Kiehl and Solomon (1986). In general, cooling rate errors of ~3% result from the 10% inaccuracy; however, there are two regions where the errors are as large as 6%, just above the stratopause and near the equatorial tropopause.

Uncertainties in gas concentration also affect the accuracy of radiative calculations. An uncertainty of 15% in the H_2O concentration produces a cooling rate uncertainty of about 0.05K day^{-1}, while uncertainties in ozone concentration ranging from 15% below 10 mb to 7% above 10 mb produce 9.6 micron band cooling rate uncertainties of up to 0.13K day^{-1} (Fels and Schwarzkopf, 1985 unpublished). On the other hand, such ozone conetration uncertainties produce ultraviolet heating rate uncertainties that are larger by as much as an order of magnitude.

7.2.5 Longwave Radiation in the Mesosphere

Moving upward from the stratopause to the vicinity of the mesopause, the problem of accurately calculating longwave cooling rates increases in complexity. Just below the stratopause, longwave transfer is dominated by cooling-to-space from the wings of nonoverlapping strong Lorentz lines of the υ_2 – funda-

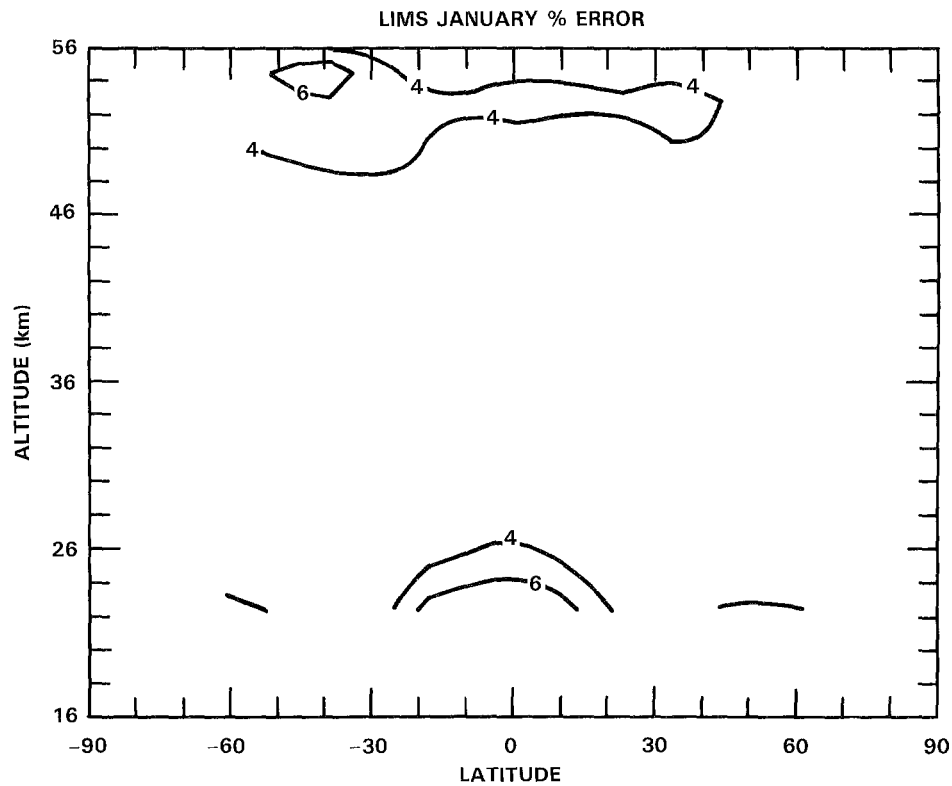

Figure 7-13. The percentage change in the LIMS January longwave cooling rates due to a 10% increase in the CO_2 line strengths.

mental of CO_2. Above the stratopause, Voigt line shapes become important, and the hot and isotopic bands of CO_2 play an increasingly important role (Dickinson, 1972, 1984; Kutepov and Shved, 1978). As the bands become more transparent looking downward as well as upward, flux divergence is no longer dominated by cooling to space, but is determined by the difference between cooling to space and warming from upwelling flux, an imbalance that can depend delicately on the vertical temperature profile. The relative contribution due to upwelling flux is strongest for the weak bands, so that this effect further enhances the importance of the hot and isotopic bands (Dickinson, 1973, 1984). However, the most important complication arises from breakdown of local thermodynamic equilibrium (LTE) for the CO_2 vibrational bands.

Since the pioneering work of Murgatroyd and Goody (1958), there have been many calculations of the longwave cooling of the mesosphere by CO_2 (e.g., Leovy, 1964b; Kuhn and London, 1969; Kutepov and Shved, 1978; Drayson, 1967; Apruzese *et al.*, 1982; Wehrbein and Leovy, 1982). All of these have followed the lead of Murgatroyd and Goody in modeling the non-LTE problem in terms of the interaction of a single vibrationally excited level and the ground state, and broadly similar cooling rate distributions have been calculated in all of these studies.

Dickinson (1984) has pointed out that this approximation may be inadequate because of the importance of the hot and isotopic bands between 60 and 85 km. These bands begin to depart noticeably from LTE around 70 km, while the more opaque fundamental remains close to LTE up to almost 80 km. Consequently a model which separately accounts for populations of $v_2 > 1$ levels of $C^{12}O_2{}^{16}$ and $v_2 = 1$ populations of minor isotopes is needed. Dickinson has carried out cooling rate calculations using a model which explicitly calculates the collisional and radiative coupling between the ground state, and the excited $v_2 = 1$ and $v_2 = 2$ levels of $C^{12}O_2{}^{16}$, as well as the $v_2 = 1$ levels of the minor CO_2 isotopes. Collisional coupling coefficients for vibrational-thermal energy exchange between $v_2 = 1$ and the ground state followed the work of Allen *et al.* (1979, 1980). The collisional coefficient coupling the $v_2 = 2$ and $v_2 = 1$ levels was taken from Taine and Lepoutre (1979). The rate for vibration-vibration exchanges of the forms

$$CO_2\ (v_2 = 2) + CO_2\ (v_2 = 0) \leftrightarrow 2\ CO_2\ (v_2 = 1)$$

and

$$CO_2\ (v_2 = 1, \text{ minor isotope}) \leftrightarrow CO_2\ (v_2 = 1, \text{ major isotope})$$

were based on a measurement of Huddleston and Weitz (1981). One vibration-vibration coupling coefficient was assumed for all of these cases, and its value is highly uncertain. Coupling between CO_2 vibrational energy and thermal energy of atomic oxygen was also included following the suggestion of Crutzen (1970), and using a coefficient based on an observation of Sharma and Nadile (1981). This coefficient is also quite uncertain, but for climatological studies the effect of atomic oxygen should be unimportant below the mesopause.

Results of Dickinson's calculation for the CIRA 1972 January-July temperature distribution are shown in Figure 7-14. It is encouraging to note that, despite the considerably greater sophistication of the model, the results are generally quite consistent with those of London (1980a), and are qualitatively similar to those of the original Murgatroyd and Goody (1958) calculations. The major uncertainties include: the temperature distribution, the vibration-vibration collisional coupling coefficients, the effect of temperature fluctuations on the calculation of climatological mean cooling rates, and the effects of collisions between atomic oxygen and CO_2 above the mesopause. Based on the uncertainties in Dickinson's calculation and the agreement between different sets of calculations, it seems that the accuracy with which long wave cooling rates due to CO_2 in the mesosphere can be calculated is about 10% or 1 K per day whichever is greater.

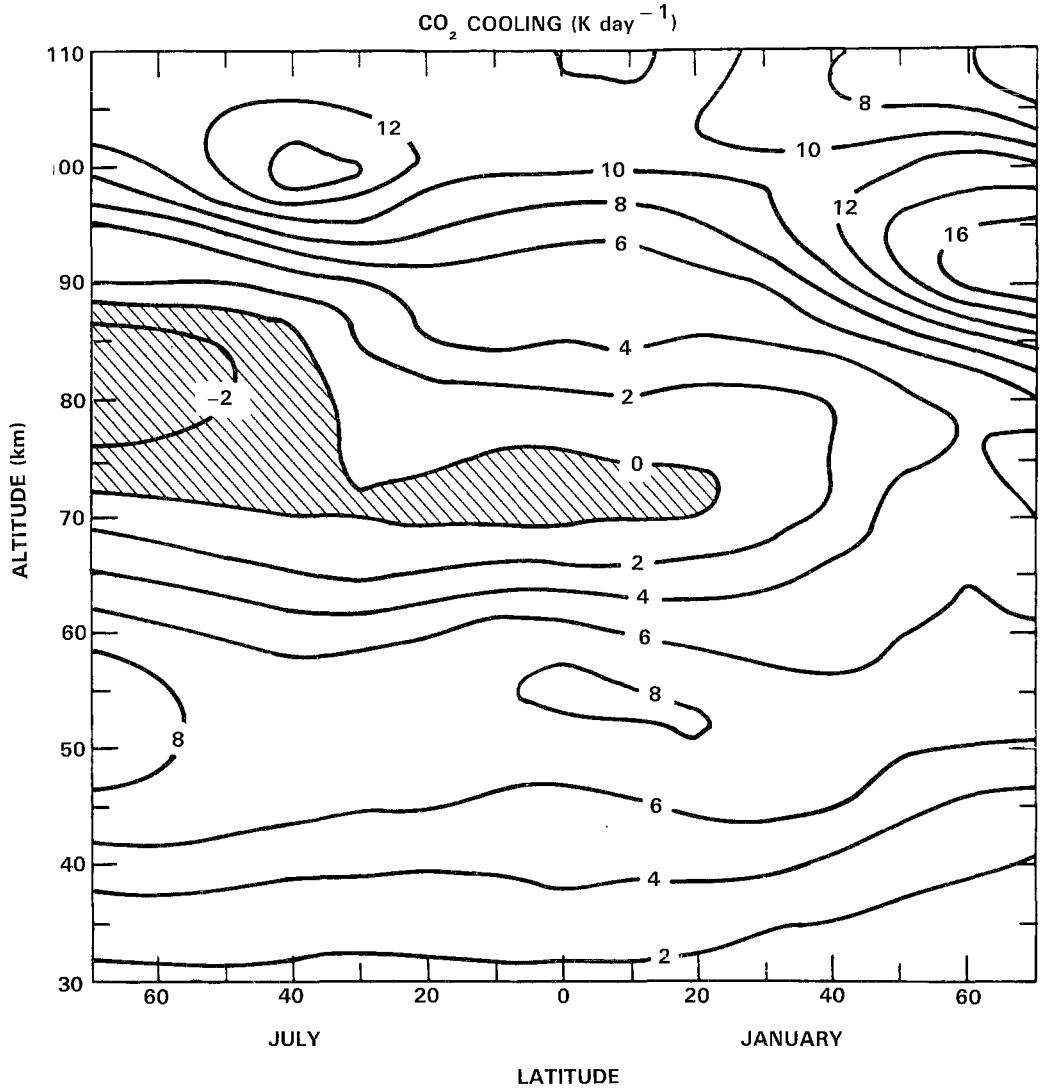

Figure 7-14. Longwave heating rate due to CO_2 in the upper stratosphere, mesosphere, and lower thermosphere for the January-July CIRA atmosphere (from Dickinson, 1984).

7.2.6 The Distribution of Net Radiative Heating

Net atmospheric heating is obtained by combining the computed long and short wave contributions. The contributions to long wave cooling and solar energy absorption have been reviewed by London (1980). It would be of interest to calculate the net heating from temperature, ozone, and water vapor distributions from a consistent global data set such as LIMS. Since the global mean net heating at any level is expected to be very close to zero, evaluation of this quantity would provide a check on the internal consistency of the data set and the other factors entering the calculations. Such a study has recently been carried out by Krehl and Solomon (1986). Except in the region between 55 and 65 km, they find global mean net cooling rate magnitudes are only a few tenths degrees Kelvin per day or less. The larger magnitudes between 55 and 65 km could be due to errors in LIMS temperatures at these altitudes. The largest uncertainty in these calculations arises from uncertainties in constituent concentrations, particularly ozone. Dickinson (1984) has evaluated the globally integrated net heating resulting from such a calculation in the mesosphere, and finds that its magnitude is generally less than 1K day^{-1}.

A second test of the accuracy of such calculations has been suggested by Fels (1985). In the summer polar stratosphere, the Eliassen-Palm flux divergence (EPFD) due to large-scale motions is very small and one expects that the net radiative heating will also be small, $\leq$ 2K day^{-1} near the stratopause. The LIMS data do not extend to the summer pole, but Fels has used a state-of-the-art radiative model to make this calculation for both a coupled radiative-photochemical model, and for observed (SBUV) ozone data. In both cases, he finds small net radiative heating rates, $<$2 K day^{-1}, near the summer stratopause.

7.3 CONCLUSIONS AND FUTURE RESEARCH NEEDS

The data base for the solar ultraviolet irradiance received at the Earth has increased tremendously both in size and quality over the last several years. This results from improved calibration techniques for rocket-borne sensors and the long term operation of instruments carried on satellites. The uncertainties in individual measurements have been estimated by the experimenters themselves and by intercomparison of results obtained by different groups. This indicates that at wavelengths between 175 and 210 nm the irradiances are known to an accuracy of $\pm$10-15% for average levels of solar activity, while between 210 and 330 nm typical error bars are 10% or less. At longer wavelengths, where measurements are obtainable from the ground, a typical uncertainty is 5% or smaller.

Instruments carried on Nimbus 7 and the Solar Mesosphere Explorer satellite have now defined the variability in solar irradiance over the 27 day rotation period of the Sun. At wavelengths between 175 and 210 nm, the spectral region important for production of odd oxygen below the mesopause, the maximum irradiance observed during a single solar rotation can be 6 to 7% above the minimum value. Longward of 210 nm out to 240 nm the minimum to maximum variation drops to 3% and by 300 nm is on the order of 1%. The variations in the core of solar emission and absorption lines can exceed these ranges. However, these fluctuations are confined to very small wavelength intervals and are therefore not important for driving variations in the Earth's atmosphere. Nonetheless, the behavior of discrete solar absorption or emission features can be valuable proxies for changes in irradiance over broad wavelength regions.

Present knowledge of variations in the 175-330 nm irradiance over the 11 year solar cycle remains inadequate. A key problem here involves identifying instrumental artifacts in the long term record obtained by satellites. As such, the reference solar cycle variation presented in this chapter should be viewed as tentative and subject to change in the future. An adequate investigation of solar cycle variability must utilize instrumentation capable of yielding a drift free data record over time scales of years to decades. The development and implementation of such a capability is identified as the major need in this research area. However, additional studies of the fundamental physical processes underlying solar variability and empirical modeling to relate observed variations to readily measurable indices of solar activity are also required.

Significant changes have taken place in accepted values of the molecular oxygen absorption cross sections at wavelengths relevant to the stratosphere and mesosphere. New laboratory data are available that provide accurate oscillator strengths and rotational line widths for the Schumann-Runge bands. These molecular parameters should now be processed into a form that allows easy use in atmospheric models. Two independent laboratory experiments have now produced consistent values of the Herzberg continuum cross section of O_2. The small values that result, being 7-8$\times$10^{-24}cm^2 near 205 nm, are compatible with most deductions from *in situ* measurements of the attenuated solar irradiance.

Absolute values of the ozone absorption cross section in the Hartley region are known to an accuracy estimated to be $\pm$2.5%. However, at wavelengths greater than 308 nm, in the Huggins bands, a compli-

cated line structure in the spectrum and a substantial temperature dependence exist. Different measurements here are difficult to compare because of the dependence of results on instrument spectral response functions. A definitive, absolute cross section measurement at very high spectral resolution would be of value here, especially for application to ground-based atmospheric ozone measurements.

For use in calculating atmospheric heating rates by solar radiation, the error bars on the incident irradiance and on the ozone and molecular oxygen absorption cross sections combine to produce a larger uncertainty in the final result than exists in any of the inputs taken alone. The error bar on the available ozone measurements themselves is probably the largest error source. A careful evaluation of the confidence level for calculated global scale solar heating rate distributions should be done based on an error analysis of all input information required in the calculations. This is especially important since dynamical models require the *net* radiative heating which is the difference between solar heating and terrestrial cooling. At many locations this difference is small compared to either component alone, and the computational errors here assume great significance.

As concerns the transfer of terrestrial radiation, present knowledge of the molecular processes and of the data required in line-by-line calculations is not completely satisfactory. The line shapes that exist in the atmosphere are determined by complex molecular interactions that are poorly modeled in the far wings. Present calculations tend to adopt Lorentz, Doppler, and Voigt line shapes that are not always accurate representations of the true state of affairs. Related to this, the pressure dependence of line shapes needs additional laboratory and theoretical study. While simple models can duplicate observed atmospheric spectra at low pressures, the agreement deteriorates as pressure increases. This issue is especially important in remote sensing of lower stratospheric composition. In addition to problems involving the shapes of atmospheric lines, additional measurements are needed of the line widths and their temperature dependencies. Additional laboratory measurements of the transmittance of bands that are relevant to the middle atmosphere would be valuable for constraining line by line calculations. The uncertainty in transmittance for some bands of minor constituents limits the accuracy with which their radiative effects can be calculated.

Calculations of longwave radiation in the stratosphere and mesosphere contain numerous uncertainties in addition to the molecular processes discussed above. The influence of clouds on the radiation balance is not yet well-defined, both as concerns the distribution and variations in cloudiness and the radiation microphysics of cloud composition. The long term significance of perturbations to the radiation budget from volcanic aerosols and stratospheric clouds is not well understood. Finally, the radiative role of trace gases such as N_2O and the chlorofluorocarbons as well as the implications of their changes over time merits further study. It is important to develop a solid quantitative understanding of all of these topics, both to adequately define all components of the radiation budget and to generate accurate net heating rates for use in studies of the atmospheric circulation.

The availability of satellite data sets for ozone, temperature, the solar irradiance, and the outgoing terrestrial emission is leading to a great increase in our understanding of the global radiation budget. It is essential that long term, accurate data sets for these important quantities continue to be collected and analyzed. This global scale information, together with information on molecular processes, is essential for developing a complete understanding of radiative processes in the Earth's stratosphere and mesosphere.